Made available through Montana State University's ScholarWorks

Mode vector modulation: receiver architectures and DSP algorithms for polarization tracking

Ioannis Roudas; Aishik Biswas; Alexander Brisson; Sina Dadras

Accessibility Disclaimer:

For a more accessible version of this document, please submit an accessibility request form through the Montana State University Library website.

Research Article Vol. 33, No. 23/17 Nov 2025/ Optics Express 47849
Optics EXPRESS

Mode vector modulation: receiver architectures and DSP algorithms for polarization tracking

IOANNIS ROUDAS,* AISHIK BISWAS, ALEXANDER BRISSON, AND SINA DADRAS

Electrical and Computer Engineering Department, Montana State University, Bozeman, MT 59717, USA
ioannis.roudas@montana.edu

Abstract: The emergence of modern hyperscale datacenters and artificial general intelligence (AGI) supercomputers creates an unprecedented demand for high-speed, scalable optical interconnects. Contemporary datacenter optical networks rely on pluggable transponders using M-ary pulse amplitude modulation (M-PAM) and direct detection (DD). To scale capacity, the prevailing strategy is to use parallel fiber strands that carry independent M-PAM/DD tributaries, a form of space-division multiplexing (SDM). Meanwhile, multicore fibers (MCFs) with nominally uncoupled, homogeneous, single-mode cores are intended to replace fiber strands in the future to reduce fiber count and simplify data center connectivity. Rather than treating each MCF core as an independent lightpath, we can exploit all MCF spatial and polarization degrees of freedom jointly to transmit multidimensional symbols via space modulation—a format we term mode vector modulation (MVM). This paper presents several novel MVM DD receiver architectures, each offering a different balance between hardware complexity and performance. In parallel, we introduce and evaluate a suite of digital signal processing (DSP) algorithms for polarization tracking, including both blind and pilot-assisted methods. Together, these innovations enhance the practicality of MVM as a high-sensitivity, bandwidth-efficient alternative to M-PAM for future direct-detection-based optical interconnects.

© 2025 Optica Publishing Group under the terms of the Optica Open Access Publishing Agreement

1. Introduction

To accommodate the exponentially increasing datacenter traffic and the demand for high-speed artificial general intelligence (AGI) supercomputer optical interconnects, pluggable transponders using M-ary pulse amplitude modulation and direct detection (M-PAM/DD) are currently being developed [1]. Experimental efforts in recent years have demonstrated the feasibility of short-haul transmission with PAM8/DD at symbol rates reaching 170 GBaud at the time of this writing [2]. Concurrently, significant progress has been made in digital signal processing (DSP) techniques for optical interconnects based on M-PAM/DD [3–5].

While M-PAM/DD optical interconnects have traditionally been preferred for short-reach links due to their low cost and simplicity, the receiver sensitivity degrades significantly with increasing constellation cardinality M. As data rates continue to rise, there is growing motivation to adopt higher-order constellations to reduce the symbol rate and confine the signal spectrum within the bandwidth limitations of commercially available components. To this end, modulation formats that are compatible with direct detection and offer enhanced receiver sensitivity relative to M-PAM are particularly attractive.

Over the years, various higher-order modulation (HOM) formats combined with direct detection have been proposed and investigated as a means to address bandwidth constraints in short-haul optical transmission systems [6,7]. These formats serve as promising interim solutions for high-speed optical interconnects in both intra- and inter-datacenter applications, bridging the gap until low-cost coherent transponders—capable of supporting a broader range of sophisticated HOM formats—become commercially viable [8].

#565232 https://doi.org/10.1364/OE.565232
Journal © 2025 Received 21 Apr 2025; revised 5 Sep 2025; accepted 9 Oct 2025; published 5 Nov 2025

Optics EXPRESS

On a broader note, the relative merits of wavelength division multiplexing (WDM) versus space division multiplexing (SDM) for scaling datacenter network capacity have been the subject of ongoing debate [9]. Historically, the high complexity and cost of WDM components have limited their adoption in datacenter environments. As a result, fiber-rich solutions allowing for a rudimentary form of SDM achieved through the use of parallel fiber lanes have been the preferred approach. Nonetheless, certain hyperscale operators have begun to deploy coarse wavelength division multiplexing (CWDM) within their datacenters, as reported in [10] and references therein.

Looking ahead, multicore optical fibers (MCFs) are poised to play an increasingly important role in datacenter infrastructure, driven by physical space constraints that limit the continuing use of discrete fiber strands [11]. By integrating multiple cores within a single cable, MCFs can significantly reduce cabling footprint and simplify connectivity management.

Nominally uncoupled, homogeneous, single-mode-core multicore fibers (MCFs) are commonly envisioned for use in datacenter environments in conjunction with space-division multiplexing (SDM), where independent data streams are transmitted through separate cores to increase overall link capacity [12].

However, the integration of MCFs in datacenters also presents an opportunity for innovation in modulation formats tailored to short-haul optical communication [13–16]. In particular, spatial modulation techniques can exploit the N spatial and polarization degrees of freedom available in uncoupled, homogeneous, single-mode-core MCFs to transmit N-dimensional symbols across the entire spatial domain. This approach contrasts with conventional SDM, where N parallel and independent data streams are transmitted through the cores [13–16].

In a recent publication [17], we investigated the potential of a novel optical interconnect paradigm based on multidimensional spatial modulation combined with self-coherent direct-detection receivers. This modulation format, referred to as mode vector modulation (MVM) [17], is denoted as (N, M)-MVM, where N represents the number of spatial and polarization degrees of freedom, and M denotes the constellation cardinality.

Table 1 contrasts the conventional M-PAM and the proposed (N, M)-MVM modulation formats, highlighting their respective strengths and limitations in the context of short-reach optical interconnects. M-PAM is favored for its simplicity, cost-effectiveness, and minimal digital signal processing (DSP) requirements, but suffers from reduced receiver sensitivity, limited scalability, and the need for elaborate polarization demultiplexing at higher data rates. In contrast, (N, M)-MVM leverages the signal space dimensionality to spread the constellation points apart in order to achieve enhanced receiver sensitivity and extended transmission reach. One of the attractive features of MVM DD receivers is their ability to perform adaptive electronic compensation of modal crosstalk. Despite these advantages, MVM suffers from increased complexity in receiver architecture, particularly due to the necessity of a large number of photodiodes and the associated analog-to-digital converters (ADCs).

In particular, the primary limitation of M-PAM lies in its one-dimensional signal space, which causes the required signal-to-noise ratio (SNR) per bit to scale quadratically with the constellation cardinality, in the amplified spontaneous emission (ASE) noise-limited regime [18]. In contrast, for (N, M)-MVM, the required SNR per bit scales as $O\left(M^{\frac{1}{N-1}}\right)$ [19], offering a significant sensitivity advantage as the number of spatial and polarization degrees of freedom increases.

However, this improvement in receiver sensitivity initially appears to come at a high cost: the number of photodiodes required for the measurement of the components of a generalized Stokes vector scales with the dimensionality of the generalized Stokes space [20], specifically as $O\left(N^2\right)$ [17]. Fortunately, a deeper analysis of the inherent interdependence among the Stokes parameters [21] reveals that all $N^2 - 1$ components of the Stokes vector can, in fact, be inferred from only $O(N)$ measurements. With recent progress in silicon photonic integrated circuits significantly reducing the cost and complexity of advanced optical receivers, we argue that MVM,

Optics EXPRESS

Table 1. Comparison of M-PAM and (N, M)-MVM modulation formats. Topics in red are addressed in this publication.

Format	Pros	Cons
M-PAM	Simplicity of implementation	Reduced receiver sensitivity
	Cost-effectiveness	Limited scalability to higher cardinalities
	Minimal DSP	Complex polarization demultiplexing
(N, M)-MVM	Multi-dimensional polarization modulation	Complex receiver architecture
	Higher sensitivity (w. geometric shaping)	Vulnerability to MD, MDL
	Electronic compensation of modal crosstalk	
	Applicability to FSOC (energy efficiency)	
	Time-domain implementation as PPM, DPSK	

when combined with self-coherent polarimetric direct detection, presents a promising pathway for realizing bandwidth-efficient, next-generation optical interconnects based on direct detection.

In this paper, which is a follow-up of [17], we elaborate on two key issues related to MVM DD receiver design (shown in red in Table 1): (i) We propose and study novel architectures for the optical front-end of MVM DD receivers with hardware complexity $O(N)$, a significant advancement that makes MVM more practical for deployment in datacenters. (ii) We introduce and evaluate multiple DSP algorithms for polarization tracking—both blind and pilot-assisted—that are specifically adapted to the MVM framework. Together, these innovations help to establish MVM as a viable, high-performance alternative to conventional M-PAM for short-reach optical interconnects.

The rest of the paper is organized as follows: Sec. 2 reviews briefly the fundamentals of MVM using generalized Jones and Stokes calculus [17]. In Sec. 3, several direct-detection receiver architectures are proposed, spanning from quadratic- to linear-hardware-complexity designs, and their performance is evaluated through simulation. In Sec. 4, DSP algorithms for polarization tracking are developed, including pilot-aided derotation, blind LMS equalization, and Wiener-Hopf filtering. Finally, Sec. 5 provides theoretical and experimental results confirming that MVM, combined with polarimetric direct detection, offers a scalable alternative to PAM4 for high-speed datacenter links.

2. Mode vector modulation: a brief overview

2.1. Literature review

Polarization shift keying (PolSK) was first investigated in the late 1980s and early 1990s [22–25], but eventually fell out of mainstream focus. In recent years, however, it has regained attention as a component of Stokes vector modulation (SVM) [26–46], fueled by advances in direct-detection systems for short-reach fiber-optic links. This renewed interest is largely attributed to the emergence of cost-effective integrated photonics and the capability to compensate for polarization rotations in optical fibers through adaptive electronic equalizers operating in Stokes space.

Stokes vector modulation (SVM) offers more power-efficient signaling than M-PAM by exploiting the full three-dimensional Stokes space, rather than the one-dimensional signal space used by M-PAM. To further enhance energy efficiency, our team extended this approach to higher-dimensional Stokes spaces by leveraging few-mode fibers, multicore fibers, or free-space modes — a technique known as mode vector modulation (MVM).

Both SVM and MVM are forms of spatial modulation formats [47]. Although they are typically paired with direct-detection receivers, spatial modulation techniques have also been investigated in coherent optical systems using multicore fibers. For instance, Eriksson et al. [13] examined multidimensional position modulation combined with various QPSK schemes

Optics EXPRESS

to enhance spectral and power efficiency. Similarly, Puttnam et al. [14–16] reviewed related approaches for high-capacity coherent and self-homodyne transmission systems.

2.2. MVM signal waveforms

MVM leverages spatial and polarization degrees of freedom in multimode fibers, multicore fibers, and free-space optical links as independent spatial channels. In this section, without loss of generality, we illustrate the concept of MVM transmission using an ideal, homogeneous two-core multicore fiber (MCF) with single-mode cores, assuming both cores are identical and exhibit negligible differential group delay.

In the illustration of Fig. 1, MVM consists in transmitting optical pulses over the two polarization states of both single-mode cores simultaneously, with each pulse having the same shape but differing in amplitude and initial phase.

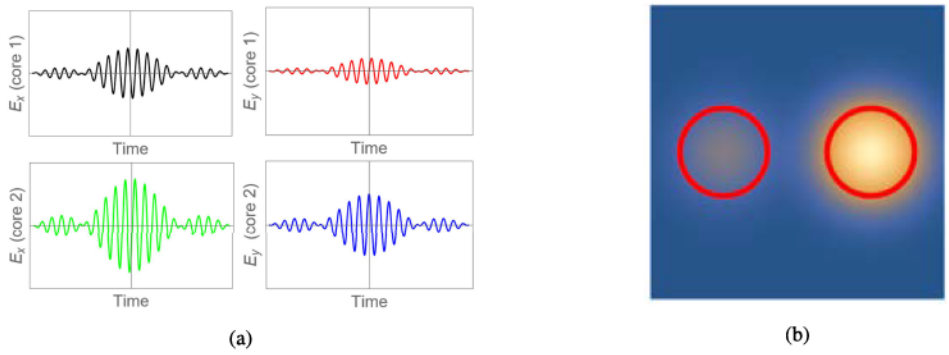


Fig. 1. (a) MVM signal waveforms transmitted over an ideal, homogeneous two-core MCF with identical, uncoupled single-mode cores; (b) Intensity distribution of the MVM symbol corresponding to the waveforms in (a).

In general, the combined optical field in MVM can be represented using $N = 2K$ polarization components — specifically, the x and y polarization states within each of the K independent cores.

The mathematical representation of MVM signals is

$$\mathbf{E}_m(t) = A_m \exp(\iota\phi_m)\, g(t)|s_m\rangle, \tag{1}$$

where $m = 1, \ldots, M$, A_m and ϕ_m represent the common amplitude and phase, respectively, $g(t)$ is a real function defining the pulse shape, and $|s_m\rangle$ is a generalized unit Jones vector that encapsulates the complex excitations across the different spatial paths, i.e., the amplitudes and phases of the electric fields of the optical waves [20,48,49].

$$|s\rangle = \begin{bmatrix} E_{x_{01}} e^{i\phi_{x_1}} \\ \vdots \\ E_{y_{0K}} e^{i\phi_{y_K}} \end{bmatrix}. \tag{2}$$

Jones vectors, up to phase, are commonly represented by generalized real Stokes vectors $\hat{s}$ in a higher-dimensional real vector space of dimension $N^2 - 1$. The generalized unit Stokes vectors

Optics EXPRESS

are defined through the quadratic form [49]

$$\hat{s} := C_N \langle s|\mathbf{\Lambda}|s\rangle, \tag{3}$$

where $\mathbf{\Lambda}$ denotes the generalized Gell-Mann matrix vector and C_N denotes the normalization coefficient [49]

$$C_N := \sqrt{\frac{N}{2\,(N-1)}}. \tag{4}$$

2.3. MVM adjacencies

It is important to note that the concepts underlying MVM extend beyond its original use as a modulation format. For instance, an interesting application involves employing MVM direct-detection receivers and DSP algorithms to facilitate polarization division multiplexing and demultiplexing in dual-polarization (DP) intensity-modulated direct-detection (IMDD) transceivers for intra-datacenter communication. In a recent experimental demonstration by Zhao et al. [50], it was shown that it is possible to achieve 400 Gbps Ethernet by launching two independent PAM4 waveforms at 100 GBaud each in the x and y states of polarization at the same wavelength. In this experiment, polarization demultiplexing was performed in the optical domain using a programmable photonic integrated circuit composed of Mach-Zehnder interferometers and phase shifters. To adjust the phase shifters, it was necessary to employ a low-speed direct-detection polarimeter. For this purpose, the four-photodiode polarimeters shown in Fig. 3 below exhibit superior performance at the thermal noise limit. In general, low-speed MVM DD transponders could be used to characterize polarization rotations in multimode/multicore fibers through pilot tones and this information can be used to control adaptive optical optical compensators.

Furthermore, in quantum networks utilizing polarization-entangled photons or spatial qudits, one could time multiplex over the same wavelength a classical MVM signal. As before, a low-speed MVM DD transponder can be used to characterize the channel through pilot tones and control an optical compensator that can compensate for polarization rotations. Then, quantum signals can be transmitted with high fidelity.

Another application could be to use MVM in high-capacity, energy-efficient free-space optical (FSO) communication links. MVM is a natural fit for FSO communication because these links are energy starved and MVM exploits the high-dimensional nature of free-space propagation to increase the receiver sensitivity.

Finally, a fundamental connection exists between SVM/MVM and multichip DPSK [51,52], based on the equivalence of spatial dimensions and time slots in the AWGN limit. Building on this relationship, we recently proposed an energy-efficient multichip DPSK scheme by representing its symbols as polarization vectors within a generalized Stokes space, allowing for optimized phase transitions and improved signal separability [53]. By permitting phase transitions to vary continuously instead of being confined to discrete $2\pi/M$ steps, we employed geometric shaping in Stokes space to increase symbol separation and lower error rates [53].

3. MVM DD receiver architectures

3.1. SVM DD receiver architectures

Initially, we review various cost-effective Stokes vector receiver architectures that offer different trade-offs between the hardware complexity of the optical front-end of the polarimetric receiver and the computational complexity of the receiver's DSP. In particular, we focus on the three widely-used contemporary SVM receivers, namely those proposed by Benedetto et al. [25], Che et al. [54], and Shieh et al. [55]. We also discuss the asymmetric hybrid SVM receiver recently proposed by our group [56,57].

Optics EXPRESS

The first SVM receiver we analyze is the one proposed by Benedetto et al. [25]. It is an analog direct-detection-based polarimeter that has been recently revamped slightly, most notably by adding a DSP unit that can perform polarization tracking [26]. The block diagram of the Benedetto receiver in its current form is shown in Fig. 2(a). At its core, it consists of three different branches of almost identical structure, composed of polarization beam splitters (PBS) and balanced photodetectors. In the second and third branches, the PBSs are preceded by polarization controllers (PCTRs) that act as half waveplates and quarter waveplates, respectively. The incoming signal state of polarization (SOP) is represented in Fig. 2(a) by the Jones vector $|r\rangle$. After a three-way splitter that divides the optical power equally among branches, the received signal SOP $|r\rangle$ is projected along the x- and y-polarization basis $|x\rangle\langle x|$ and $|y\rangle\langle y|$, the linear 45°- and the −45°- polarization basis $|45°\rangle\langle 45°|$ and $|-45°\rangle\langle -45°|$, and the right-circular (RC)- and left-circular (LC)- polarization basis $|RC\rangle\langle RC|$ and $|LC\rangle\langle LC|$, respectively. The power difference between the two orthogonal SOPs of each arm is equal to the Stokes parameter of the incoming signal along the main axis of the corresponding PBS. Using the Jones-Stokes calculus, we can show that the photocurrents at the outputs of the balanced receiver can be used to calculate the normalized Stokes vector [58].

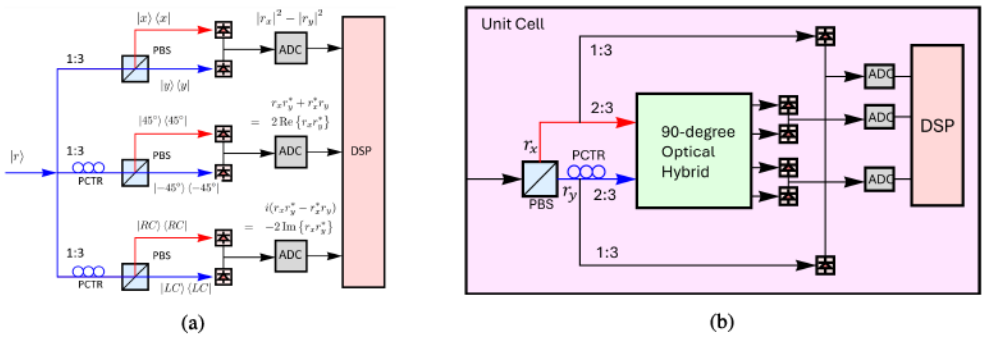


Fig. 2. (a) The conventional direct-detection-based polarimeter SVM receiver [25]; (b) A phase-diversity SVM receiver that is more amenable to photonic integration [54]; PCTR: polarization controller, PBS: polarization beam splitter, ADC: analog-to-digital converter.

A seemingly different, but mathematically equivalent variant of the same architecture is shown in Fig. 2(b). It uses a phase-diversity receiver composed of a 90-degree optical hybrid and two balanced detectors, and was first proposed by Che et al. [54]. A 90-degree optical hybrid is a multiport coupler routinely used in phase-diversity coherent optical intradyne receivers to mix the optical signals of the transmitter and the local oscillator prior to photodetection. A PCTR placed at the input of the optical hybrid aligns both polarization tributaries created by the PBS to the same state of polarization. The upper and lower balanced detectors after the optical hybrid in Fig. 2(b) measure the real and imaginary part of the product of the incoming optical signals, respectively. The DSP combines these terms to create the $s_i s_j^*$ terms. Several recent hero experiments such as [30] use the direct-detection SVM receiver architecture depicted in Fig. 2(b), because this configuration is more amenable to photonic integration since it uses a 90-degree optical hybrid to combine the incoming optical signals.

Shieh et al. [55] proposed a cost-effective direct-detection SVM receiver architecture using four single-ended photodetectors (PDs) (Fig. 3(a)). The receiver comprises a 2×2 asymmetric coupler (in blue) in cascade with a 3×3 optical hybrid (in green) as shown in Fig. 3(a).

Another cost-effective SVM receiver architecture, based on an asymmetric optical hybrid and four single-ended photodiodes, is shown in Fig. 3(b) [57]. We call this the Asymmetric Hybrid Receiver (AHR). The asymmetric optical hybrid is depicted inside the rectangular boxes in Fig. 3(b). It consists of two asymmetric directional 2×2 couplers (green), two directional

Optics EXPRESS

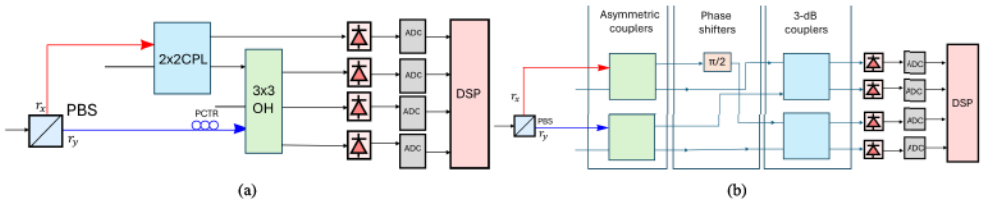


Fig. 3. (a) A cost-effective SVM receiver that uses only four photodiodes [55]; (b) The four-photodiode asymmetric hybrid SVM receiver [56,57]; CPL: coupler, OH: 90-degree optical hybrid, PBS: polarization beam splitter, PCTR: polarization controller, ADC: analog to digital converter.

2×2 3-dB couplers (blue), a 90° phase shifter, and a fiber permutation between stages. The two beam splitters at the input of the optical hybrid are not 50:50 splitters, but have an unequal power splitting ratio $\gamma/(1-\gamma)$, where γ is a free parameter to be adjusted for optimum receiver performance.

3.2. *Previously-proposed MVM DD receivers*

The SVM receiver architecture proposed by Che at al. [54] (Fig. 2(b)) can be easily generalized for N>2 giving rise to the conventional, quadratic-complexity MVM receiver. The receiver estimates the dyad of the received signal $|r\rangle\langle r|$, which is an $N \times N$ Hermitian matrix. A Hermitian matrix is equal to its own conjugate transpose. Off-diagonal elements form complex conjugate pairs symmetrically across the main diagonal. Therefore, it is sufficient to measure only the elements in the upper triangular part of the dyad. The upper triangular part of the dyad has N real elements at the diagonal and $N(N-1)/2$ complex off-diagonal elements. We need N single-ended photodiodes to measure the N diagonal elements and $N(N-1)/2$ optical hybrids each having four photodiodes to measure the $N(N-1)/2$ off-diagonal elements. The total number of photodiodes in this receiver type is thus $2N^2 - N$.

For illustration, in Fig. 4(a), we show the schematic of an optical-hybrid-based quadratic-complexity MVM receiver for the special case of $N = 4$. This receiver could be used, for instance, together with a two-core MCF with identical single-mode cores. The design consists of two PBSs at the output of the single-mode cores, respectively, followed by four power splitters, six 90-degree optical hybrids (each with two balanced photodiodes), and four single-ended photodiodes, therefore equaling a grand total of 28 photodiodes, in accordance with the formula $2N^2 - N$. The PBSs split the optical signal into its $x-$ and $y-$ components, and the power splitters divide the incoming power into four parts based on an optimal splitting criterion. PCTRs at the inputs of the optical hybrids turn both polarization tributaries into the same polarization. Like discussed earlier, the most unsophisticated implementation of the MV receiver for the detection of generalized Stokes vectors requires a total of $2N^2 - N$ identical photodiodes. The disadvantage of this architecture is that its complexity scales quadratically with N. It is possible to design a more sophisticated MVM DD receiver architecture [21] that exploits the interdependence of the generalized Stokes parameters to reduce the front-end complexity. This reduced architecture for the special case of $N = 4$ is shown schematically in Fig. 4(b). The basic building block (and associated optical components) of this receiver is the same as the full-fledged receiver with a couple of notable differences. The most profound difference is the reduced number of 90-degree optical hybrids, which results in a lower number of photodiodes. While the number of optical hybrids in the quadratic complexity receiver is $N(N-1)/2$, the number of hybrids in the new linearized-complexity receiver is only $N-1$. This is because the $N^2 - 1$ Stokes components are functions of the N Jones components and are interdependent, thus making inference of a large number of Stokes parameters possible given a small number of measurements. We can conclude

Optics EXPRESS

by noting that since each optical hybrid has two pairs of balanced photodiodes (four photodiodes in total) and additionally, N single-ended photodiodes are required to measure the $|s_i|^2$ terms, a total of $5N-4$ photodiodes are required. For the $N=4$ case, this translates to a total of 16 photodiodes as seen in Fig. 4(b).

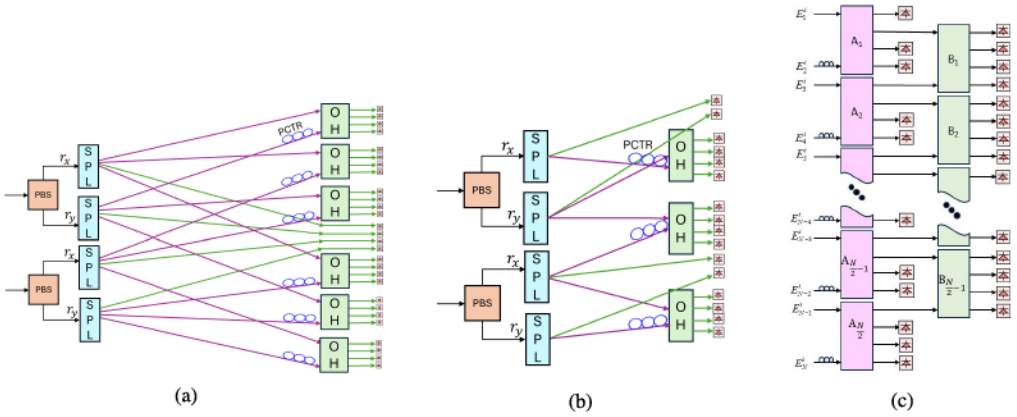


Fig. 4. (a) The full-fledged quadratic complexity MVM receiver for $N=4$; (b) A linearized-complexity MVM receiver for $N=4$ having $5N-4$ photodiodes; (c) The asymmetric hybrid MVM receiver for arbitrary N, composed of cascaded asymmetrical optical hybrid and $3N-2$ photodiodes; PBS: polarization beam splitter, SPL: power splitter, OH: 90-degree optical hybrid, PCTR: polarization controller.

The previously-discussed AHR can be generalized to any even N as shown in Fig. 4(c). This architecture requires $N/2$ input hybrids (magenta), with the first and last connected to 3 photodiodes, and the remaining $N/2-2$ hybrids connected to 2 photodiodes each. These are followed by $N/2-1$ output optical hybrids (green), each connected to 4 photodiodes. This design results in a total of $N-1$ asymmetric optical hybrids and only $3N-2$ photodiodes. These measurements are sufficient to recover the (N^2-1)-dimensional Stokes vector as described in detail in [56].

3.3. *Novel MVM receiver architectures with linear-hardware-complexity*

The hardware complexity of the conventional MVM direct detection receiver scales quadratically with the number of modes N leading to a decrease in cost-effectiveness with increasing N. This drawback could significantly hinder the adoption of MVM in short-haul communications despite its superior receiver sensitivity compared to conventional modulation formats such as M-PAM. Over the past couple of years, we have proposed various cost-effective MVM receiver architectures that have linear-hardware-complexity [21,56,57]. While these receivers have been shown to match the performance of the quadratic-complexity MVM receiver in the optically amplified regime, they greatly lag behind the quadratic-complexity MVM receiver in the thermal-noise-limit for $N>2$ [56,57]. In this paper, we present two new MVM receiver designs with linear-hardware-complexity that aim to enhance the performance at the thermal-noise-limit while preserving their cost-effectiveness. This endeavor is particularly important, as it is thermal noise that limits the sensitivity of MVM direct-detection receivers in the absence of optical amplification.

3.3.1. New receiver-design I using $4N$ photodiodes

A novel receiver architecture for mode vector direct-detection that has a total of N asymmetric optical hybrids and $4N$ photodiodes is shown in Fig. 5(a). The asymmetric hybrids used in this

Optics EXPRESS

design are the same as reported in [56,57] and shown within the rectangle in Fig. 3(b). However, unlike the asymmetric hybrid receiver (AHR) in [56,57], the present design uses only one layer of N asymmetric hybrids. Each asymmetric optical hybrid can be described by a 4×4 unitary transfer matrix, which relates the input and output electric field vectors $|E^i\rangle$ and $|E^o\rangle$ as

$$|E^o\rangle = \begin{bmatrix} E_1^o \\ E_2^o \\ E_3^o \\ E_4^o \end{bmatrix} = \frac{1}{\sqrt{2}} \begin{bmatrix} bE_1^i + aE_2^i \\ bE_1^i - aE_2^i \\ iaE_1^i + bE_2^i \\ iaE_1^i - bE_2^i \end{bmatrix}, \tag{5}$$

where a and b are the amplitude splitting ratios of the asymmetric couplers inside the asymmetric hybrid (Fig. 3(b)) where $a^2 + b^2 = 1$. Note that $a^2/b^2 = (1-\gamma)/\gamma$, where γ is the power splitting ratio referred to earlier in the paper. The value of the splitting ratio is set to its optimum value calculated analytically for $N = 2$ in [56] at the thermal-noise-limit. The optimum a, b and γ are given by:

$$a = \sqrt{\frac{1}{6}(3 \pm \sqrt{3})}, b = \sqrt{\frac{1}{6}(3 \mp \sqrt{3})}, \gamma = \frac{1}{6}(3 \mp \sqrt{3}). \tag{6}$$

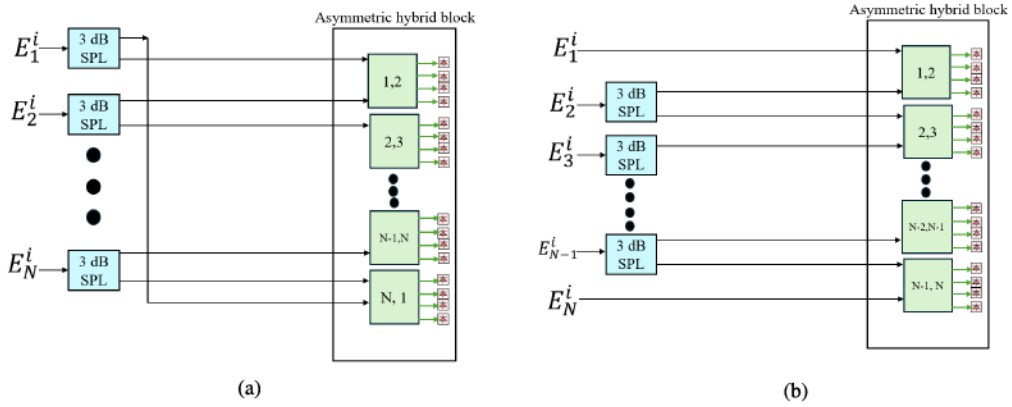


Fig. 5. (a) Schematic of the optical front-end of an MVM receiver with $4N$ photodiodes for any even N; (b) Schematic of the optical front-end of an MVM receiver with $4(N-1)$ photodiodes for any even N.

To understand the DSP necessary to calculate the generalized Stokes parameters, consider the special case corresponding to $N = 4$ where the optical front-end comprises four 3 dB splitters and four asymmetric hybrids. For $N = 4$, the $N^2 - 1 = 15$ elements of the generalized Stokes

Optics EXPRESS

vector can be written in terms of the electric fields as shown in (7).

$$\begin{bmatrix}
\sqrt{\frac{2}{3}}\left(E_1^i E_2^{i*} + E_2^i E_1^{i*}\right) \\
\sqrt{\frac{2}{3}}\left(E_1^i E_3^{i*} + E_3^i E_1^{i*}\right) \\
\sqrt{\frac{2}{3}}\left(E_2^i E_3^{i*} + E_3^i E_2^{i*}\right) \\
\sqrt{\frac{2}{3}}\left(E_1^i E_4^{i*} + E_4^i E_1^{i*}\right) \\
\sqrt{\frac{2}{3}}\left(E_2^i E_4^{i*} + E_4^i E_2^{i*}\right) \\
\sqrt{\frac{2}{3}}\left(E_3^i E_4^{i*} + E_4^i E_3^{i*}\right) \\
\sqrt{\frac{2}{3}}\left(E_1^i E_2^{i*} - E_2^i E_1^{i*}\right) \\
\sqrt{\frac{2}{3}}\left(E_1^i E_3^{i*} - E_3^i E_1^{i*}\right) \\
\sqrt{\frac{2}{3}}\left(E_2^i E_3^{i*} - E_3^i E_2^{i*}\right) \\
\sqrt{\frac{2}{3}}\left(E_1^i E_4^{i*} - E_4^i E_1^{i*}\right) \\
\sqrt{\frac{2}{3}}\left(E_2^i E_4^{i*} - E_4^i E_2^{i*}\right) \\
\sqrt{\frac{2}{3}}\left(E_3^i E_4^{i*} - E_4^i E_3^{i*}\right) \\
\sqrt{\frac{2}{3}}\left(E_1^i E_1^{i*} - E_2^i E_2^{i*}\right) \\
\sqrt{\frac{2}{3}}\left(\frac{E_1^i E_1^{i*}}{\sqrt{3}} + \frac{E_2^i E_2^{i*}}{\sqrt{3}} - \frac{2E_3^i E_3^{i*}}{\sqrt{3}}\right) \\
\sqrt{\frac{2}{3}}\left(\frac{E_1^i E_1^{i*}}{\sqrt{6}} + \frac{E_2^i E_2^{i*}}{\sqrt{6}} + \frac{E_3^i E_3^{i*}}{\sqrt{6}} - \sqrt{\frac{3}{2}}E_4^i E_4^{i*}\right)
\end{bmatrix}. \tag{7}$$

Each of the generalized Stokes parameters in (7) can be determined by inferring the elements of the dyad shown in (8).

$$|E^i\rangle\langle E^i| = \begin{bmatrix}
|E_1^i|^2 & E_1^i E_2^{i*} & E_1^i E_3^{i*} & E_1^i E_4^{i*} \\
E_2^i E_1^{i*} & |E_2^i|^2 & E_2^i E_3^{i*} & E_2^i E_4^{i*} \\
E_3^i E_1^{i*} & E_3^i E_2^{i*} & |E_3^i|^2 & E_3^i E_4^{i*} \\
E_4^i E_1^{i*} & E_4^i E_2^{i*} & E_4^i E_3^{i*} & |E_4^i|^2
\end{bmatrix}. \tag{8}$$

The elements in blue are estimated directly from the four output photocurrents in each asymmetric hybrid in Fig. 5(a). Let us consider the first asymmetric hybrid and deduce how its output photocurrents can be used to estimate certain blue elements of the dyad (8). Given the responsivity R of the photodiodes, the photocurrents can be mapped to the optical powers at the four outputs, defined as $P_k := |E_k^o|^2$. Substituting the output electric fields from (5), the output powers are obtained as

$$2P_1 = b^2|E_1^i|^2 + a^2|E_2^i|^2 + 2ab\,\mathrm{Re}\{E_1^i E_2^{i*}\}, \tag{9a}$$

$$2P_2 = b^2|E_1^i|^2 + a^2|E_2^i|^2 - 2ab\,\mathrm{Re}\{E_1^i E_2^{i*}\}, \tag{9b}$$

$$2P_3 = a^2|E_1^i|^2 + b^2|E_2^i|^2 - 2ab\,\mathrm{Im}\{E_1^i E_2^{i*}\}, \tag{9c}$$

$$2P_4 = a^2|E_1^i|^2 + b^2|E_2^i|^2 + 2ab\,\mathrm{Im}\{E_1^i E_2^{i*}\}. \tag{9d}$$

In the absence of noise, summing these four expressions gives $\sum_{k=1}^{4} P_k = 1$, since we assume normalized Jones vectors, i.e., $|E_1^i|^2 + |E_2^i|^2 = 1$. From these measured powers, our objective is

Optics EXPRESS

to determine the terms $|E_1^i|^2$, $|E_2^i|^2$, and $E_1^i E_2^{i*}$, which are elements of the dyad (8). Solving (9) for these terms yields

$$|E_1^i|^2 = \frac{a^2(P_3+P_4) - b^2(P_1+P_2)}{a^2-b^2}, \tag{10a}$$

$$|E_2^i|^2 = \frac{a^2(P_1+P_2) - b^2(P_3+P_4)}{a^2-b^2}, \tag{10b}$$

$$E_1^i E_2^{i*} = \frac{(P_1-P_2) + i(P_4-P_3)}{2ab}. \tag{10c}$$

Similarly, by using the output photocurrents from the other three asymmetric hybrids and appropriately modifying the indices in (10a)–(10c), additional blue elements of the dyad can be inferred.

Note that each of the diagonal elements $|E_j^i|^2$ where $j \leq N$ in (8) can be independently calculated from the output photocurrents of two distinct asymmetric hybrids using (10a) and (10b). For example, in the case $N = 4$, the element $|E_1^i|^2$ can be inferred from both the first asymmetric hybrid (which combines E_1^i and E_2^i) and the fourth asymmetric hybrid (which combines E_4^i and E_1^i). Instead of simply ignoring one of these extra measurements, we take their average and use it to compute the dyad. Since both hybrids are implemented with identical components, their thermal noise variances are approximately equal (σ^2). Moreover, because the noise originates from physically distinct photodiodes and resistors, the two contributions are uncorrelated, i.e. $\mathrm{cov}(n_1, n_2) = 0$. Under these assumptions, the variance of the averaged estimate is reduced by half, $\mathrm{var}\left(\frac{X_1+X_2}{2}\right) = \frac{\sigma^2}{2}$, which directly improves the effective SNR of the diagonal terms. We initially hypothesized that by utilizing each measurement and computing their averages, we would be able to increase the noise robustness and reduce error propagation. Subsequently, via simulations we verified that taking the average slightly boosted the receiver sensitivity compared to the case where we only utilized one of the measurements.

The elements in green are then calculated from the elements in blue using an iterative process first reported in [21]. This algorithm is based on the fact that the $N^2 - 1$ Stokes components are functions of the N Jones components and are interdependent, making inference of a large number of Stokes parameters possible given a small number of measurements. In other words, a pair of distinct products $E_i E_j^*$, $E_j E_k^*$ contain common information as they share a common Jones component E_j. The first step is to calculate the differential phases $\theta_{i,i+1}$, where

$$\theta_{i,i+1} := \theta_i - \theta_{i+1} = \arg\left(E_i E_{i+1}^*\right). \tag{11}$$

In the case $N = 4$, this refers to the phases $\theta_{1,2}$, $\theta_{2,3}$, and $\theta_{3,4}$. Since the terms $E_1^i E_2^{i*}$, $E_2^i E_3^{i*}$, and $E_3^i E_4^{i*}$ (shown in blue in the dyad (8) are already known, the differential phase terms can easily be inferred. Thus, we can now retrieve all remaining terms $E_i E_j^*$ by

$$E_i E_j^* = e^{i\theta_{i,j}} |E_i||E_j|, \tag{12}$$

where, for any $i<j$,

$$\theta_{i,j} := \theta_{i,i+1} + \cdots + \theta_{j-1,j}. \tag{13}$$

For our special case of $N = 4$, the remaining terms of the required form (shown in green in (8) are $E_1^i E_3^{i*}$ and $E_2^i E_4^{i*}$. These two terms can be easily calculated using (12) and (13) since we already know the required diagonal elements as well as the differential phases.

Finally, the elements in black are inferred by using the fact that they are simply complex conjugates of elements that have been previously determined. Thus, we have demonstrated how each element of the dyad $|r\rangle\langle r|$ is determined for $N = 4$. This method can be easily extended to

Optics EXPRESS

any even N. From the dyad $|r\rangle\langle r|$, the DSP can evaluate the generalized Stokes vector (7) based on the formulae (3), (4).

It is worth discussing how thermal noise affects the various elements of the dyad (8). As seen in (10a)–(10b), the diagonal elements $|E_j^i|^2$ are obtained from additive combinations of photocurrents, yielding strong signal terms; moreover, because each diagonal can be computed from two distinct asymmetric hybrids, we average the two independent estimates, which halves the noise variance and further improves robustness. In contrast, the off-diagonal in (10c) (nearest-neighbor, e.g., $E_1^i E_2^{i*}$ in (8) is formed directly from differences of nearly balanced photocurrents (e.g., $P_1 - P_2$ and $P_4 - P_3$), so the useful signal partially cancels while the thermal noise variances add, producing a much lower effective SNR. For other cross terms (12) (e.g., $E_1^i E_3^{i*}$ in (8), we reconstruct the complex quantity as $E_i E_j^* = |E_i||E_j|\, e^{i(\theta_{i,i+1}+\cdots+\theta_{j-1,j})}$, so multiple noisy differential phases are summed and their uncertainties accumulate in the exponential. Consequently, these off-diagonal entries are inherently more susceptible to thermal noise than the diagonal powers, and the DSP stage, which combines these noisy phase estimates, makes the disparity appear more pronounced.

3.3.2. New receiver-design II using $4(N-1)$ photodiodes

On close inspection of the receiver architecture and the corresponding DSP outlined in the last section, it becomes evident that there exists some redundancy in the design. In particular, it is inferred that the last hybrid does not yield any new information that is not already computable via the measurements of the other hybrids. Specifically, in the case $N = 4$, the dyad element $E_4^i E_1^{i*}$ need not be measured from the fourth hybrid like we did earlier; instead, it can be inferred using the same procedure explained earlier for the receiver with $4N$ photodiodes [21].

At first, we calculate $E_1 E_4^*$ by modifying (12) and (13) as shown below.

$$E_1 E_4^* = e^{i\theta_{1,4}} |E_1||E_4|, \tag{14}$$

where

$$\theta_{1,4} = \theta_{1,2} + \theta_{2,3} + \theta_{3,4}. \tag{15}$$

Since the necessary electric fields and the differential phases from (14) and (15) above are already known as explained above for the $4N$ receiver, $E_4^i E_1^{i*}$ and its complex conjugate $E_1^i E_4^{i*}$ can be easily determined without having to use an additional asymmetric hybrid. As a result, the last hybrid can be omitted, giving rise to a receiver with $N-1$ hybrids and $4(N-1)$ photodiodes. Note that all other elements of the dyad are calculated exactly as were calculated for the receiver with $4N$ photodiodes with suitable scaling factors added as explained below. The optical front-end of this receiver is shown in Fig. 5(b).

Notice that in Fig. 5(b), the first and last inputs do not have 3 dB splitters, unlike the inputs in the middle. This power asymmetry in the architecture needs to be compensated in the DSP by employing suitable scaling factors for the elements of the dyad $|r\rangle\langle r|$. Let us assume that the dyad elements (8) measured from the various asymmetric hybrids as explained earlier prior to any scaling are denoted using e's instead of E's. Like in the $4N$ design, there are certain elements in the dyad that can be independently derived from the outputs of two different asymmetric hybrids. These correspond to the $N-2$ central terms in the main diagonal, which are each calculated from the addition $|e_{k,j}^i|^2 + |e_{k,j+1}^i|^2$ in two successive hybrids where k is the index of the E-field and and j is the index of the asymmetric hybrid. This addition serves as an averaging mechanism to reduce errors as described in the previous section, while at the same time compensating for the power asymmetry described above. Secondly, the multiplying factors for the $N-3$ terms in the second diagonal are 2, and for the two edge terms, they are $\sqrt{2}$. The dyad for $N = 4$ after applying the necessary scaling is shown below in (16). Like in the previous architecture, the dyad elements are calculated in the order blue, green, and black. Like in the $4N$ case, the blue

Optics EXPRESS

elements denote the ones measured directly from the output photocurrents of the asymmetric hybrids and the green elements are determined from the blue elements using an iterative process explained in detail in the previous section [21]. The element in black are once again determined by noting that they are the complex conjugates of the blue and green elements.

$$|E^i\rangle\langle E^i| = \begin{bmatrix} |e_1^i|^2 & \sqrt{2}e_1^i e_2^{i*} & e_1^i e_3^{i*} & e_1^i e_4^{i*} \\ e_2^i e_1^{i*} & |e_{2,1}^i|^2 + |e_{2,2}^i|^2 & 2e_2^i e_3^{i*} & e_2^i e_4^{i*} \\ e_3^i e_1^{i*} & e_3^i e_2^{i*} & |e_{3,2}^i|^2 + |e_{3,3}^i|^2 & \sqrt{2}e_3^i e_4^{i*} \\ e_4^i e_1^{i*} & e_4^i e_2^{i*} & e_4^i e_3^{i*} & |e_4^i|^2 \end{bmatrix}. \tag{16}$$

After applying the appropriate scaling, we can compute the correct dyad (16), which allows us to evaluate the generalized Stokes vector (7) based on the formulae (3), (4). Thus, we have described another novel receiver architecture for mode vector direct detection that has a total of $N-1$ asymmetric optical hybrids and only $4(N-1)$ photodiodes. The two aforementioned receiver architectures have been compared on the basis of important metrics in Table 2. We can clearly see that there exists a tradeoff between hardware complexity/cost and computational complexity of the DSP.

Table 2. Comparison of the two receiver architectures proposed in this paper.

Metric	Receiver I	Receiver II
Photodiode count	$4N$	$4(N-1)$
Asymmetric hybrid count	N	$N-1$
Upfront cost	More	Lower
DSP	Less dependence/less computational complexity	More dependence/more computational complexity

4. Adaptive polarization tracking in the generalized Stokes space

As an MVM signal travels along an optical fiber, its state of polarization is perturbed and rotated. Successful reception of an MVM signal therefore requires counteracting these distortions in order to correctly determine the received symbol. Further complicating the matter is that the fiber rotation varies over time due to environmental changes, e.g., temperature fluctuations and vibrations. The goal of this section is to show how such rotations can be counteracted within the MVM receiver's DSP.

4.1. Correspondence of rotation matrices in Jones and Stokes spaces

Consider an N-dimensional Jones space and a $D = (N^2-1)$-dimensional Stokes space. Rotations within Jones space are given by $|t\rangle = \mathbf{U}|s\rangle$ for a unitary Jones matrix $\mathbf{U}$, while rotations within Stokes space are given by $\hat{t} = \mathbf{R}\hat{s}$ for a Müller matrix $\mathbf{R}$. We can calculate the Müller matrix $\mathbf{R}$ from the Jones matrix $\mathbf{U}$ from the formula

$$\mathbf{R}_{ij} = \frac{1}{2}\mathrm{tr}\left[\mathbf{U}^\dagger \lambda_i \mathbf{U} \lambda_j\right] \tag{17}$$

where λ_i, λ_j denote the generalized Gell-Mann matrices.

Proof. Letting $|s\rangle$ and $\hat{s}$ denote the same state of polarization in Jones and Stokes space respectively, we will perform the rotations $|t\rangle = \mathbf{U}|s\rangle$ and $\hat{t} = \mathbf{R}\hat{s}$ and seek to relate the resulting

Optics EXPRESS

terms. We begin by recalling that the components of the Stokes vector $\hat{s}$ are given by (3), (4)

$$\hat{s}_k = C_N \langle s|\lambda_k|s\rangle, \quad C_N = \sqrt{\frac{N}{2(N-1)}}, \tag{18}$$

where λ_k is a generalized Gell-Mann matrix. Using that $|t\rangle = \mathbf{U}|s\rangle$ and converting to Stokes space yields

$$\hat{t}_i = C_N \langle t|\lambda_i|t\rangle = C_N \langle s|\mathbf{U}^\dagger \lambda_i \mathbf{U}|s\rangle, \tag{19}$$

while using $\hat{t} = \mathbf{R}\hat{s}$ yields

$$\hat{t}_i = \sum_k \mathbf{R}_{ik}\hat{s}_k = \sqrt{\frac{N}{2(N-1)}} \sum_k \mathbf{R}_{ik} \langle s|\lambda_k|s\rangle = C_N \left\langle s \middle| \sum_k \mathbf{R}_{ik}\lambda_k \middle| s \right\rangle. \tag{20}$$

Equating these two expressions for $\hat{t}_i$ yields that

$$\langle s|\mathbf{U}^\dagger \lambda_i \mathbf{U}|s\rangle = \left\langle s \middle| \sum_k \mathbf{R}_{ik}\lambda_k \middle| s \right\rangle. \tag{21}$$

As this equation holds for arbitrary $|s\rangle$, we arrive at the matrix equation

$$\mathbf{U}^\dagger \lambda_i \mathbf{U} = \sum_k \mathbf{R}_{ik}\lambda_k, \tag{22}$$

which yields

$$\mathbf{U}^\dagger \lambda_i \mathbf{U}\lambda_j = \sum_k \mathbf{R}_{ik}\lambda_k\lambda_j \tag{23}$$

upon right-multiplication by λ_j. Taking the trace of both sides, while noting that $\mathrm{tr}\left[\lambda_k\lambda_j\right] = 2\delta_{kj}$, gives that

$$\mathrm{tr}\left[\mathbf{U}^\dagger \lambda_i \mathbf{U}\lambda_j\right] = \sum_k \mathbf{R}_{ik}\mathrm{tr}\left[\lambda_k\lambda_j\right] = \sum_k \mathbf{R}_{ik}2\delta_{kj} = 2\mathbf{R}_{ij} \tag{24}$$

and thus

$$\mathbf{R}_{ij} = \frac{1}{2}\mathrm{tr}\left[\mathbf{U}^\dagger \lambda_i \mathbf{U}\lambda_j\right] \tag{25}$$

as desired.

4.2. Pilot-based derotation

The *pilot symbol derotation scheme* hinges upon the observation that the fiber rotation, while varying over time, is approximately constant on the time scale of a symbol period. We can therefore periodically send K predetermined ***pilot symbols*** to characterize the fiber, estimate the rotation matrix, and thus derotate subsequent symbols carrying the data payload. This method does incur an overhead and thus reduce the effective data transmission rate, but the exact amount of pilot symbols in relation to data symbols will depend on the engineering application.

Letting $\hat{s}_k$ and $\vec{t}_k$ denote the k-th symbol transmitted and received, and $\vec{n}_k$ denote a noise vector we have

$$\vec{t}_k = \mathbf{R}\hat{s}_k + \vec{n}_k, \tag{26}$$

for the unknown Müller matrix $\mathbf{R}$ (which is assumed to be constant over the timescale of interest). In the following, we omit the noise in (26). Collecting the first $K \geq D$ symbols to characterize

Optics EXPRESS

the fiber, we create the auxiliary matrices

$$\mathbf{T} := \begin{bmatrix} | & & | \\ \vec{t}_1 & \dots & \vec{t}_K \\ | & & | \end{bmatrix}, \quad \mathbf{S} := \begin{bmatrix} | & & | \\ \hat{s}_1 & \dots & \hat{s}_K \\ | & & | \end{bmatrix} \tag{27}$$

The Stokes space rotation for all K symbols can be written in compact form

$$\mathbf{T} = \mathbf{RS}, \tag{28}$$

where the dimensions of matrices are $D \times K$, $D \times D$, and $D \times K$, respectively. We can estimate $\mathbf{R}$ using the pseudo-inverse:

$$\mathbf{R} = \mathbf{TS}^T(\mathbf{SS}^T)^{-1}, \tag{29}$$

where we note that $\mathbf{SS}^T$ is invertible provided that $\mathbf{S}$ is full rank. As we have complete control over the chosen $K \geq D$ pilot symbols, this condition is easily satisfied.

Having thus characterized the fiber rotation via the Müller matrix $\mathbf{R}$, we can derotate subsequent symbols $\vec{t}_k$, $k>K$, arriving at the receiver the by computing the derotated symbol $\mathbf{R}^{-1}\vec{t}_k \approx \hat{s}_k$ in the DSP.

4.3. *Blind adaptive channel equalization in Stokes space*

The mode vector direct-detection receiver DSP can estimate and counteract Stokes vector rotations caused by fiber propagation using blind adaptive channel equalization.

4.3.1. Least-mean squares (LMS) algorithm

Blind adaptive channel equalization can be performed using the least-mean squares (LMS) algorithm (Fig. 6(a)).

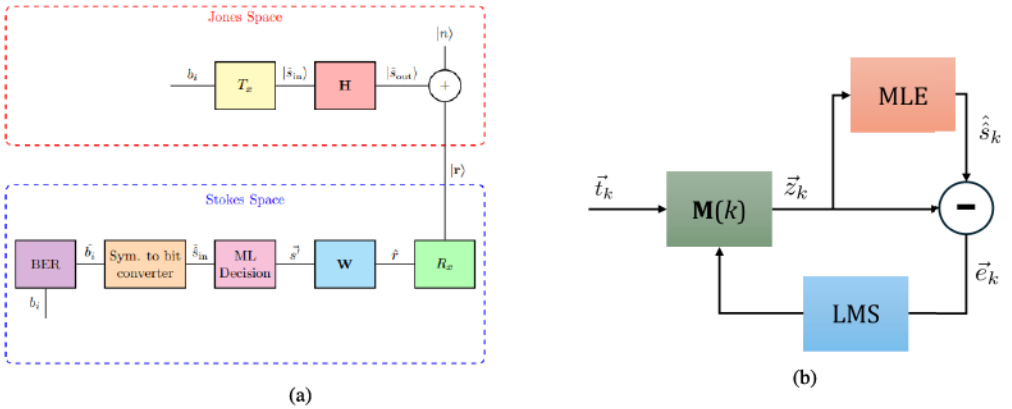


Fig. 6. (a) Block diagram of MVM transceiver; (b) Least-mean squares (LMS) blind adaptive channel equalizer. Abbreviations and symbol definitions: b_i= input bit, T_x=transmitter, $|\hat{s}_{in}\rangle$= input Jones vector, $|n\rangle$= noise in Jones space, $\mathbf{H}$= channel transfer matrix, $|\hat{s}_{out}\rangle$= output Jones vector, $|r\rangle$= output vector with noise in Jones space, R_x= receiver, $\hat{r}$= output vector with noise in Stokes space, $\mathbf{W}$= derotator, $\vec{s}'$= Stokes vector after the derotation, ML= maximum likelihood, $\hat{\vec{s}}_{in}$= estimated Stokes vector, $\hat{b}_i$= estimated input bit, BER= bit error rate.

In Fig. 6(a), the received generalized Stokes vector $\vec{t}_k$ is multiplied at the $k-$th time instant with a compensating generalized $(N^2-1)\times(N^2-1)$ Müller matrix $\mathbf{M}(k)$. The resulting generalized

Optics EXPRESS

Stokes vector $\vec{z}_k$ is used by the maximum-likelihood decision criterion to estimate the transmitted Stokes vector $\hat{s}_k$. The estimated Stokes vector is denoted by a double hat $\hat{\hat{s}}_k$. The error signal between the derotated generalized Stokes vector $\vec{z}_k$ and the estimated symbol $\hat{\hat{s}}_k$ is given by their difference. The LMS equalizer uses the mean square error (MSE) as its cost function

$$\xi = E\{\|\vec{e}_k\|^2\}. \tag{30}$$

We want to minimize the cost function (30) by recursively adjusting the elements of the Müller matrix $\mathbf{M}(k)$ in Fig. 6(a).

The conventional LMS algorithm replaces the expectation $E\{\|\vec{e}_k\|^2\}$ in (30) by its instantaneous value $\|\vec{e}_k\|^2$. Expanding the norm we obtain

$$\xi_k = \|\vec{e}_k\|^2 = \|\hat{\hat{s}}_k - \vec{z}_k\|^2 = 1 + \|\vec{z}_k\|^2 - 2\hat{\hat{s}}_k \cdot \vec{z}_k. \tag{31}$$

We need to calculate the gradient of the above cost function, which requires the partial derivatives of ξ_k with respect to the elements of the matrix M_{ij}. We assume that, to the first-order, the estimated symbol $\hat{\hat{s}}_k$ is not affected by small changes in the values of M_{ij}. Therefore, we only need to evaluate the partial derivatives of the terms that contain $\vec{z}_k$ with respect to the elements of the matrix M_{ij}.

$$\nabla\xi = \left[\frac{\partial\xi}{\partial M_{ij}}\right], \tag{32}$$

where

$$\frac{\partial\xi}{\partial M_{ij}} \simeq 2\left(\vec{z}_i - \hat{\hat{s}}_i\right)\vec{t}_j. \tag{33}$$

Rewriting the gradient-descent method in matrix formulation, we obtain

$$\mathbf{M}(k+1) = \mathbf{M}(k) - \mu\nabla\xi_k = \mathbf{M}(k) - 2\mu\left[\vec{z}_k - \hat{\hat{s}}_k\right] \otimes \vec{t}_k, \tag{34}$$

where $\otimes$ denotes the outer product.

4.4. Derotation based on Wiener-Hopf equation

In this section, we derive an analytical expression for the optimal derotation matrix based on the theory of Wiener filters [59].

We assume that we transmit Stokes vectors $\mathbf{S}$ and we receive their rotated noisy versions $\mathbf{T} = \mathbf{RS}$ as given by (28). The receiver performs a derotation of $\mathbf{T}$ by multiplying them with a matrix $\mathbf{M}$ that we want to evaluate based on a mathematically-tractable optimality criterion.

As an objective function for the optimality of the derotation, we use the mean-squared error criterion

$$\xi := E\left\{\mathrm{tr}\left(\mathcal{E}\mathcal{E}^T\right)\right\}, \tag{35}$$

where $E\{.\}$ denotes expectation (i.e., ensemble averaging) and we defined the error $\mathcal{E}$ between the ideal output Stokes vector $\mathbf{S}$ and the actual output Stokes vector after derotation $\mathbf{MT}$ as

$$\mathcal{E} := \mathbf{S} - \mathbf{MT}. \tag{36}$$

The outer product of the error vector with itself is written as

$$\begin{aligned}\mathcal{E}\mathcal{E}^T &= (\mathbf{S} - \mathbf{MT})(\mathbf{S} - \mathbf{MT})^T \\ &= \mathbf{SS}^T + \mathbf{MTT}^T\mathbf{M}^T - \mathbf{ST}^T\mathbf{M}^T - \mathbf{MTS}^T\end{aligned} \tag{37}$$

Optics EXPRESS

By using (37) in (35) and by interchanging the order of the expectation function and the trace, the objective function is given by

$$\begin{aligned}\xi = \mathrm{tr}\left[E\left\{\mathbf{S}\mathbf{S}^T\right\} + \mathbf{M}E\left\{\mathbf{T}\mathbf{T}^T\right\}\mathbf{M}^T\right.\\ \left. - E\left\{\mathbf{S}\mathbf{T}^T\right\}\mathbf{M}^T - \mathbf{M}E\left\{\mathbf{T}\mathbf{S}^T\right\}\right].\end{aligned} \tag{38}$$

We set the autocorrelation matrices:

$$\mathbf{K_S} := E\left\{\mathbf{S}\mathbf{S}^T\right\}, \tag{39a}$$

$$\mathbf{K_T} := E\left\{\mathbf{T}\mathbf{T}^T\right\}, \tag{39b}$$

$$\mathbf{P} := E\left\{\mathbf{S}\mathbf{T}^T\right\}. \tag{39c}$$

By substituting (39) into (38), we obtain

$$\begin{aligned}\xi &= \mathrm{tr}\left[\mathbf{K_S} + \mathbf{M}\mathbf{K_T}\mathbf{M}^T - \mathbf{P}\mathbf{M}^T - \mathbf{M}\mathbf{P}^T\right],\\ &= \mathrm{tr}\left[\mathbf{K_S}\right] + \mathrm{tr}\left[\mathbf{M}\mathbf{K_T}\mathbf{M}^T\right] - \mathrm{tr}\left[\mathbf{P}\mathbf{M}^T\right] - \mathrm{tr}\left[\mathbf{M}\mathbf{P}^T\right].\end{aligned} \tag{40}$$

We will show that the optimum derotation matrix is

$$\boxed{\mathbf{M} = \mathbf{P}\mathbf{K}_\mathbf{T}^{-1},} \tag{41}$$

which is a variant of the Wiener-Hopf equation [59].

Proof. To simplify the proof, we will use the Einstein summation convention, i.e., when an index variable appears twice in a single term, it implies summation of that term over all the values of the index. For instance, the trace of a matrix is calculated by taking the sum of the diagonal elements of the resulting matrix. Using the Einstein summation convention, we write for brevity $\mathrm{tr}\mathbf{C} = \mathbf{C}_{ii}$ instead of $\mathrm{tr}\mathbf{C} = \sum_i \mathbf{C}_{ii}$. Similarly, for matrix multiplication, the elements of the product $\mathbf{C} = \mathbf{A}\mathbf{B}$ are written for brevity as $\mathbf{C}_{ij} = \mathbf{A}_{ik}\mathbf{B}_{kj}$ instead of $\mathbf{C}_{ij} = \sum_k \mathbf{A}_{ik}\mathbf{B}_{kj}$.

To obtain the elements $\mathbf{M}_{\mu\nu}$ of the optimum derotation matrix $\mathbf{M}$, we minimize the objective function ξ by setting the partial derivatives of ξ with respect to all $\mathbf{M}_{\mu\nu}$ to zero

$$\frac{\partial \xi}{\partial \mathbf{M}_{\mu\nu}} = 0. \tag{42}$$

We define the auxiliary cost functions

$$\xi_1 := \mathrm{tr}\left[\mathbf{M}\mathbf{K_T}\mathbf{M}^T\right] = \mathrm{tr}\left[\mathbf{K_T}\mathbf{M}^T\mathbf{M}\right], \tag{43a}$$

$$\xi_2 := \mathrm{tr}\left[\mathbf{P}\mathbf{M}^T\right], \tag{43b}$$

$$\xi_3 := \mathrm{tr}\left[\mathbf{M}\mathbf{P}^T\right]. \tag{43c}$$

Switching the order of the matrices inside the trace and using the Einstein summation convention, we can rewrite ξ_1 in terms of the elements of $\mathbf{K_T}$, $\mathbf{M}^T$, and $\mathbf{M}$ as follows:

$$\xi_1 := \mathrm{tr}\left[\mathbf{M}\mathbf{K_T}\mathbf{M}^T\right] = \mathrm{tr}\left[\mathbf{K_T}\mathbf{M}^T\mathbf{M}\right] = \mathbf{K}_{\mathbf{T}_{ik}}\mathbf{M}^T_{km}\mathbf{M}_{mi} = \mathbf{K}_{\mathbf{T}_{ik}}\mathbf{M}_{mk}\mathbf{M}_{mi}. \tag{44}$$

Taking the partial derivative of ξ_1 with respect to $\mathbf{M}_{\mu\nu}$, we obtain

$$\frac{\partial \xi_1}{\partial \mathbf{M}_{\mu\nu}} = \mathbf{K}_{\mathbf{T}_{ik}}\delta_{m\mu}\delta_{k\nu}\mathbf{M}_{mi} + \mathbf{K}_{\mathbf{T}_{ik}}\mathbf{M}_{mk}\delta_{m\mu}\delta_{i\nu}, \tag{45}$$

where δ_{ij} denotes the Kronecker delta.

Optics EXPRESS

Simplifying the Kronecker deltas, we obtain

$$\frac{\partial \xi_1}{\partial \mathbf{M}_{\mu\nu}} = \mathbf{K}_{\mathbf{T}_{i\nu}} \mathbf{M}_{\mu i} + \mathbf{K}_{\mathbf{T}_{\nu k}} \mathbf{M}_{\mu k} \tag{46}$$

Changing the dummy variable for summation in the second term from k to i and taking into account the symmetry of the matrix $\mathbf{K_T}$ that yields $\mathbf{K}_{\mathbf{T}_{\nu i}} = \mathbf{K}_{\mathbf{T}_{i\nu}}$, we obtain

$$\frac{\partial \xi_1}{\partial \mathbf{M}_{\mu\nu}} = \mathbf{K}_{\mathbf{T}_{i\nu}} \mathbf{M}_{\mu i} + \mathbf{K}_{\mathbf{T}_{\nu i}} \mathbf{M}_{\mu i} = \mathbf{K}_{\mathbf{T}_{i\nu}} \mathbf{M}_{\mu i} + \mathbf{K}_{\mathbf{T}_{i\nu}} \mathbf{M}_{\mu i} = 2\mathbf{K}_{\mathbf{T}_{i\nu}} \mathbf{M}_{\mu i}, \tag{47}$$

or, equivalently,

$$\frac{\partial \xi_1}{\partial \mathbf{M}_{\mu\nu}} = 2\mathbf{K}_{\mathbf{T}_{i\nu}} \mathbf{M}_{\mu i} = 2\mathbf{M}_{\mu i} \mathbf{K}_{\mathbf{T}_{i\nu}}, \tag{48}$$

which can be written in matrix form as

$$\frac{\partial \xi_1}{\partial \mathbf{M}} = 2\mathbf{M}\mathbf{K}_{\mathbf{T}}. \tag{49}$$

Similarly, since $\xi_2 := \mathrm{tr}\left[\mathbf{P}\mathbf{M}^T\right] = \left(\mathbf{P}\mathbf{M}^T\right)_{ii} = \mathbf{P}_{ik}\mathbf{M}^T_{ki} = \mathbf{P}_{ik}\mathbf{M}_{ik}$, taking the partial derivative of ξ_2 with respect to $\mathbf{M}_{\mu\nu}$, we obtain

$$\frac{\partial \xi_2}{\partial \mathbf{M}_{\mu\nu}} = \delta_{i\mu}\delta_{k\nu}\mathbf{P}_{ik} = \mathbf{P}_{\mu\nu}. \tag{50}$$

Finally, since $\xi_3 := \mathrm{tr}\left[\mathbf{M}\mathbf{P}^T\right] = \left(\mathbf{M}\mathbf{P}^T\right)_{ii} = \mathbf{M}_{ik}\mathbf{P}^T_{ki} = \mathbf{M}_{ik}\mathbf{P}_{ik}$, taking the partial derivative of ξ_2 with respect to $\mathbf{M}_{\mu\nu}$, we obtain

$$\frac{\partial \xi_3}{\partial \mathbf{M}_{\mu\nu}} = \delta_{i\mu}\delta_{k\nu}\mathbf{P}_{ik} = \mathbf{P}_{\mu\nu}. \tag{51}$$

Assembling everything together, we get

$$\frac{\partial \xi}{\partial \mathbf{M}} = 2\left(\mathbf{M}\mathbf{K}_{\mathbf{T}} - \mathbf{P}\right) = \mathbf{0}, \tag{52}$$

or, equivalently,

$$\boxed{\mathbf{M} = \mathbf{P}\mathbf{K}_{\mathbf{T}}^{-1}.} \tag{53}$$

5. Results and discussion

5.1. Performance of MVM DD receivers under noise and transmission impairments

First, we compute the performance of our proposed receivers through Monte Carlo simulations in the exclusive presence of thermal noise for $N = 4$ and $N = 6$. We compare our two proposed receivers with the quadratic complexity MVM receiver consisting of $2N^2 - N$ photodiodes (Fig. 4(a)), which is a generalization of the receiver reported in [54] for N>2, the linear complexity receiver proposed by us in [21], which uses $5N - 4$ photodiodes (Fig. 4(b)), as well as the AHR (Fig. 4(c)), which employs $3N - 2$ photodiodes [56,57]. The BER vs. launch power curves for all these receivers in the thermal-noise-limited regime are shown in Fig. 7(a) and Fig. 7(b). From Fig. 7(a) ($N = 4$), we see that in the thermal-noise-limit, the receiver with $4N$ photodiodes significantly outperforms all other linear-complexity receivers including the one with $4(N - 1)$ photodiodes. In particular, employing the receiver with $4N$ photodiodes instead of the AHR boosts the sensitivity by ≈ 2 dB. It still lags behind the quadratic-complexity receiver by ≈ 2

Optics EXPRESS

dB, which is a vastly reduced margin than its competitors. One of the reasons for the superiority of the receiver with $4N$ photodiodes over the AHR despite both being based on asymmetric hybrids is the fact that the former's splitting ratio is optimized while the latter's is not. This is because the receiver with $4N$ photodiodes is based on a set of cascaded asymmetric hybrids each corresponding to $N = 2$. The splitting ratio of the asymmetric couplers in the receiver with $4N$ photodiodes for any even N is set to its optimum value at the thermal-noise-limit for $N = 2$ as shown in (6) and derived analytically in [56]. However, for the AHR, computing the optimum splitting ratios for $N>2$ is a non-trivial problem and we have to resort to repeated numerical computations that are not exact leading to reduced receiver sensitivity.

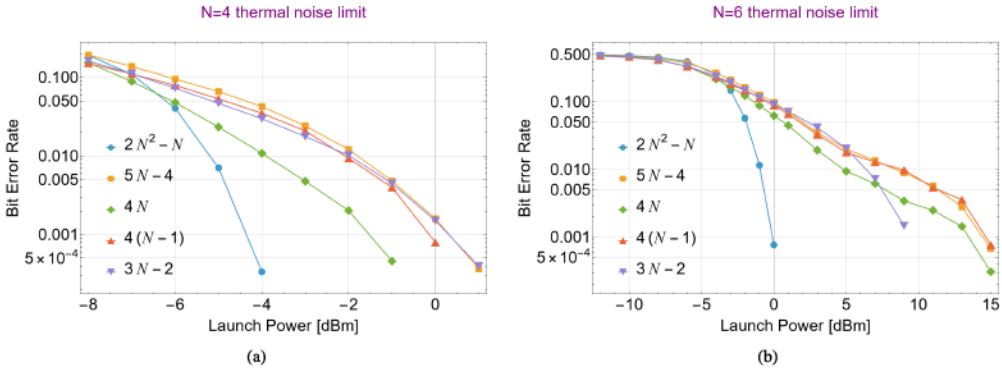


Fig. 7. BER vs. launch power for different receiver types in the exclusive presence of thermal noise at a bit rate of 10 Gb/s. (a) (4, 16)-MVM; (b) (6, 64)-MVM.

Additionally, we can conclude that reducing the number of photodiodes from $4N$ to $4(N-1)$ results in a significant performance penalty, which diminishes its feasibility despite being more cost-efficient. The reason for the lower receiver sensitivity of the receiver with $4(N-1)$ photodiodes is its greater dependence on error-prone DSP as opposed to direct measurements as outlined in Table 2. However, for $N = 6$ (Fig. 7(b)), the gain associated with the receiver bearing $4N$ photodiodes observed in Fig. 7(a) disappears for higher SNRs. Interestingly, in Fig. 7(b), we observe that at higher SNRs, the probability of error versus SNR plot for the two receivers proposed in this paper does not resemble a waterfall curve in a log-log diagram but rather a double waterfall, i.e., it displays a floor at certain intermediate SNR values. This phenomenon is also observed for the receiver with $5N-4$ photodiodes [21]. These findings lead us to conclude that thermal noise greatly affects the inference of the $E_iE_j^*$ terms of the received field dyad (8), (16) in the linear complexity receivers for $N>2$, and this effect becomes more pronounced as we increase N and thus reduce the number of direct measurements and rely more heavily on the DSP. The unequal effect of thermal noise on different dyad elements has been discussed in detail in section 3.3.1. We also note that the AHR with $3N-2$ photodiodes begins to outperform the other linear-complexity schemes at launch powers above approximately 3 dBm. While the exact mechanism behind this crossover is not fully understood, one possible explanation is that the reduced detector count in the AHR alters the balance between noise averaging and nonlinear distortion at higher input powers. At the same time, other receiver configurations may be more prone to error propagation or numerical instabilities in the DSP at high powers, which could account for their comparatively degraded performance.

In Fig. 8(a) and Fig. 8(b), we compare the performance of our two proposed receivers with an ideal receiver as well as the conventional, quadratic-complexity receiver with $2N^2-N$ photodiodes in the presence of amplified spontaneous emission (ASE) noise and modal dispersion (MD). These simulations were conducted in a 6-mode few-mode fiber (FMF), using a set of linear coupled-mode equations as described in [60]. Within the MVM transmitter, ideal root

Optics EXPRESS

raised cosine (RRC) waveforms corresponding to the geometrically optimized (6, 64)-MVM constellation are generated. The system parameters include a total fiber length of 10 km, a symbol rate of 56 GBd, a mode coupling coefficient of −30 dB/km, and no intramodal dispersion between the polarization components of the LP_{01} and LP_{11} modes. To facilitate optical compensation, half of the fiber length is configured with a Differential Mode Delay (DMD) of the opposite sign. Additionally, a DSP unit employs a least mean square (LMS) algorithm [17] to mitigate polarization rotations in Stokes space induced during fiber propagation. The results clearly show that the new receivers with $4N$ and $4(N-1)$ photodiodes do not cause any additional penalty with respect to the ideal/conventional MVM receivers both in the presence and in the absence of optical compensation.

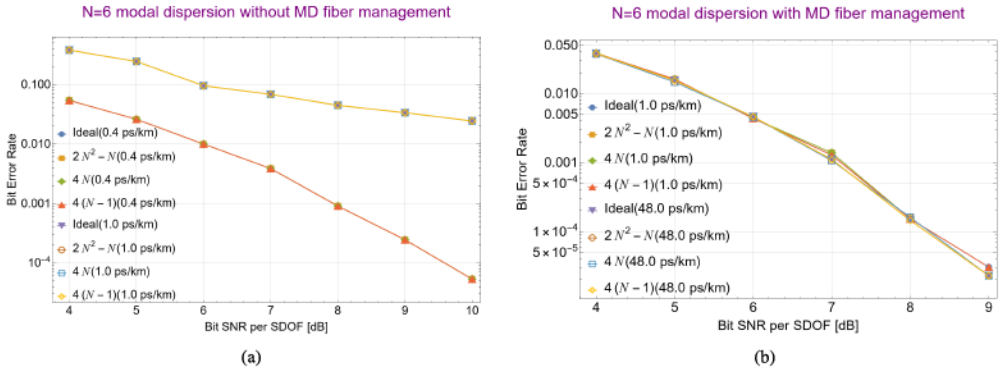


Fig. 8. BER vs. bit SNR per spatial degree of freedom for different receiver types considering the impact of intermodal dispersion for (6, 64)-MVM at a symbol rate of 56 GBd. (a) Without MD fiber management; (b) With MD fiber management.

Now that we have verified that all receiver architectures are equivalent in terms of receiver sensitivity in the presence of MD, ASE noise, and intermodal coupling, it is worth investigating how transmission distance affects the performance of MV-DD receivers. The three transmission distances we simulate are 1 km, 5 km, and 10 km, all of which are realistic fiber-optic link lengths in short-haul optical links such as inter- and intra- data center links and short-reach data center interconnects (DCIs). In Fig. 9(a), as expected intuitively, we observe that the BER increases as we increase the transmission distance at a constant MD parameter of 1 ps/km and no optical compensation. In Fig. 9(b), we observe that transmission distance does not have a significant effect on the performance of MV-DD receivers at a MD parameter of 48 ps/km and in the presence of optical compensation. This is because, the optical compensation described earlier almost perfectly neutralizes the effect of MD even at longer transmission distances and stronger MD. In both the scenarios, we assumed a mode coupling coefficient of −30 dB/km and a symbol rate of 56 GBd.

Besides intermodal dispersion, another important effect in MV-DD systems is spatial mode coupling as well as its single mode counterpart: polarization mode coupling. In the preceding simulations, we have considered a mode coupling coefficient of −30 dB/km, which introduces undesirable intermodal crosstalk between the various spatial modes in our FMF. In Fig. 10(a) and Fig. 10(b), we quantify the effect of varying levels of intermodal coupling on the performance of our two proposed MVM receivers both in the presence and in the absence of DMD management. In the absence of DMD fiber management (Fig. 10(a)), we see that with a constant low MD parameter of 0.4 ps/km, the impact of varying intermodal crosstalk remains negligible up to at least -10 dB/km. This is because the effects of uncompensated DMD appear to overshadow any potential penalty from crosstalk. When MD increases to 24 ps/km, and DMD fiber management is employed (Fig. 10(b)), the influence of crosstalk becomes more pronounced but still tolerable. As

Optics EXPRESS

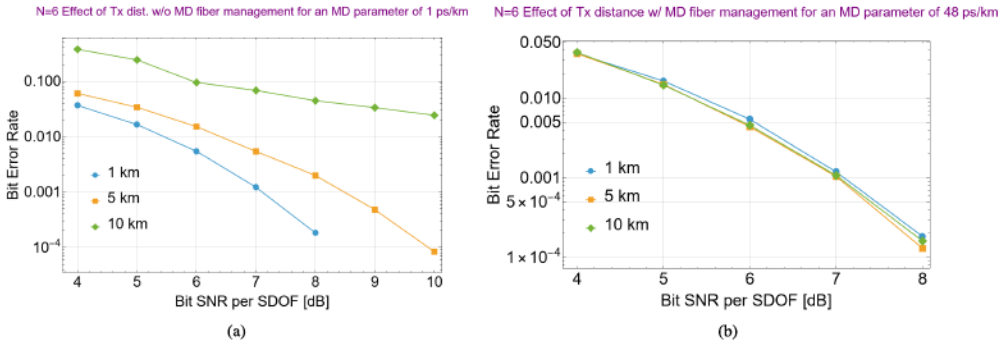


Fig. 9. BER vs. bit SNR per spatial degree of freedom considering the impact of transmission distance for (6, 64)-MVM at a symbol rate of 56 GBd. (a) Without MD fiber management; (b) With MD fiber management.

seen in Fig. 10(b), the BER rises as the degree of modal crosstalk increases from -40 dB/km to -10 dB/km. This crosstalk-induced degradation in performance is due to the accumulation of modal crosstalk before DMD compensation, which contains significantly large DMD corresponding to a MD parameter of 24 ps/km. The combined effects of large DMD and crosstalk result in power coupling between larger arrays of adjacent symbol components of the three propagating modes, leading to greater penalties at the receiver. Overall, the two proposed receivers exhibit equivalent receiver sensitivity in this regime, even in the presence of significant modal crosstalk. It is worth noting that polarization mode coupling in single-mode systems is mathematically analogous to spatial mode coupling in FMF/MCF, since both manifest as linear mixing between tributaries. Prior work on direct-detection MIMO receivers similar to ones we used has shown that such polarization coupling can be effectively tolerated with only minor BER penalties [61]. This further supports our finding that realistic levels of modal or polarization coupling do not fundamentally limit the proposed architectures in short-reach links.

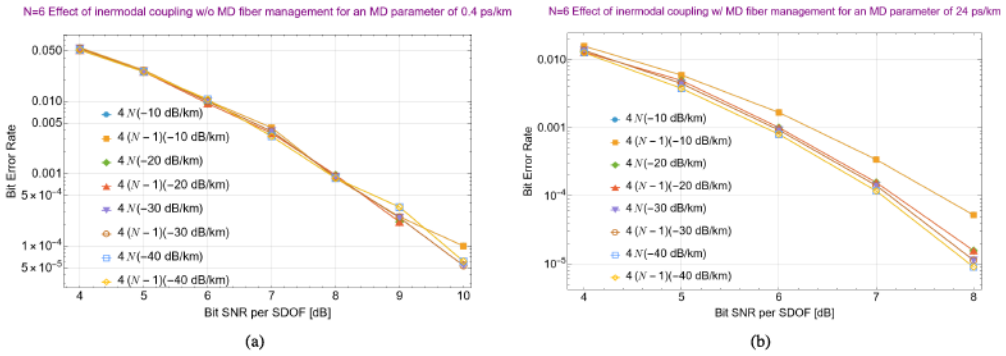


Fig. 10. BER vs. bit SNR per spatial degree of freedom considering the impact of varying levels of spatial mode coupling for (6, 64)-MVM at a symbol rate of 56 GBd. (a) Without MD fiber management; (b) With MD fiber management.

These aforementioned simulations neglected the effect of fiber chromatic dispersion (CD), which is a valid assumption when operating in the O-band [62]. Nevertheless, it is worth quantifying the effect of CD on our proposed MVM receivers when operating in both the C-band and the O-band since our receivers are not equipped to compensate for CD. In the subsequent simulations, we assume that CD is the dominant impairment and ASE noise and thermal noise is negligible. We also note that the effects of MD are perfectly counteracted through optical

Optics EXPRESS

compensation as explained earlier and that we are in the low intermodal coupling regime where the effects of modal crosstalk are negligible. These assumptions enable us to isolate the effect of CD and characterize the CD tolerance of the proposed receivers. Like earlier, we consider a total fiber length of 10 km and a symbol rate of 56 GBd. In Fig. 11(a) and Fig. 11(b), we see how the BER changes with varying accumulated CD ($D \times L$) for (4, 16)-MVM and (6, 64)-MVM transmission in the C-band where D is the chromatic dispersion coefficient and L is the fiber length. We see that at 56 GBd in C-band, the proposed receivers tolerate up to 30 ps/nm accumulated CD before the BER degrades steeply. At 1550 nm, with typical SMF $D \approx 16.7$ ps/nm/km, that tolerance equals only ≈ 1.8 km of uncompensated fiber. Thus, for longer links, it is imperative to transition to the O-band where the chromatic dispersion coefficient D is extremely small. At O-band (~1312 nm), 10 km of SMF corresponds to less than 20 ps/nm accumulated dispersion. Across this entire range, the receivers showed no measurable errors. Thus, in the intended O-band scenario, CD is negligible and does not limit performance. Additionally, from Fig. 11(a) and Fig. 11(b), it is evident that the two proposed receivers are equivalent in the exclusive presence of CD.

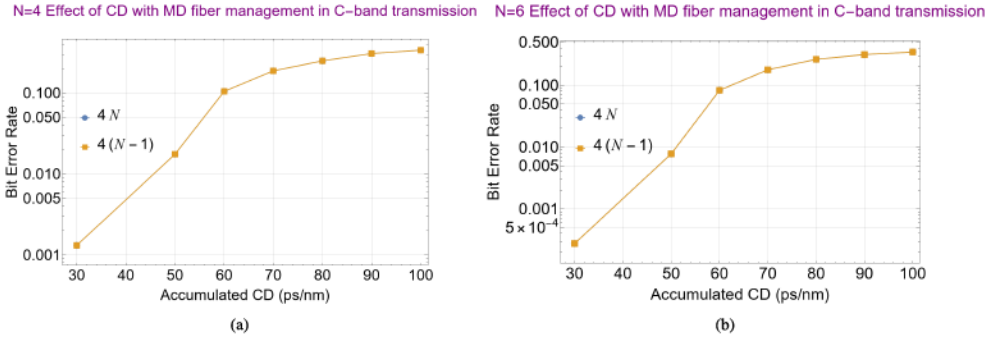


Fig. 11. BER vs. accumulated CD for the two proposed receiver types in the C-band at a symbol rate of 56 GBd. (a) (4, 16)-MVM.; (b) (6, 64)-MVM.

5.2. *DSP algorithm validation*

5.2.1. Pilot-aided polarization derotation using an LMS equalizer

To evaluate the convergence behavior of the LMS algorithm and its sensitivity to Additive White Gaussian Noise (AWGN), numerical simulations were conducted using a 4-SVM signal in a back-to-back configuration without fiber impairments.

A random 3×3 rotation matrix $\mathbf{R}$ was generated to model polarization rotation in Stokes space. This matrix was derived via singular value decomposition (SVD) of a normally distributed random matrix $\mathbf{A}$. The resulting unitary matrix $\mathbf{R}$ was used to simulate symbol rotations by evaluating $\hat{t}_k = \mathbf{R}\hat{s}_k$. Additive noise $\vec{n}_k$ was generated to simulate received signals as $\vec{t}_k = \hat{t}_k + \vec{n}_k$. Figures 12(a) and 12(b) illustrate the pilot-aided LMS algorithm's performance in estimating the Müller matrix $\mathbf{M}(k)$ under varying SNR.

Figure 12(a) shows the evolution of the average cost function $\bar{\xi}$ over 1,000 pilot symbols and an n-symbol moving average, i.e., $\bar{\xi}_k := \frac{1}{n}\sum_{i=0}^{n-1} \xi_{k-i}$. AWGN imposes a lower bound on $\bar{\xi}$, limiting the LMS algorithm's accuracy in producing the optimum $\mathbf{M}(k)$. This is evident in Fig. 12(b), where the derotated Stokes vectors (blue) do not perfectly overlap with the transmitted vectors (black), indicating residual error.

The optimal step size μ of the LMS algorithm varies depending on noise conditions, as shown in Fig. 13. A robust estimate of μ can be obtained by averaging cost-function performance over many random realizations of $\mathbf{R}$. For benchmarking against the pseudo-inverse, the LMS

Optics EXPRESS

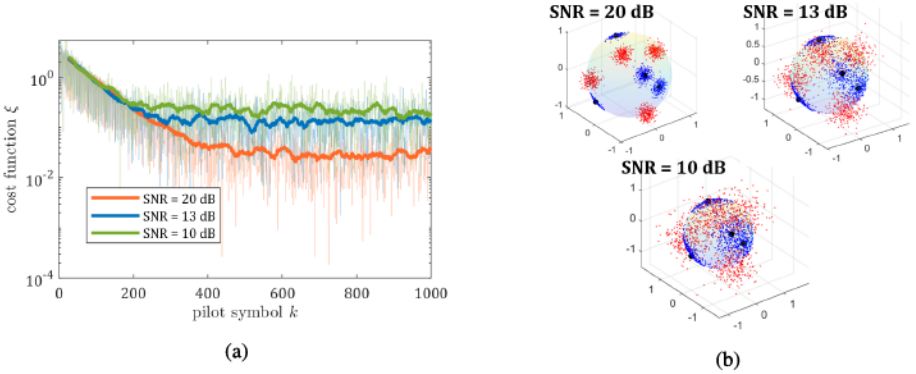


Fig. 12. Pilot-aided LMS results with step size $\mu = 0.01$. (a) Average cost function $\bar{\xi}$ minimized using $k = 1,000$ pilots across SNRs. The light shaded traces represent ξ, whereas the bolded traces represent $\bar{\xi}$ with $n = 25$. (b) Poincaré spheres showing transmitted ($\hat{s}_k$, black), received ($\vec{t}_k$, red), and derotated (blue) Stokes vectors.

algorithm may be applied to derotate a 4-SVM constellation using a fixed-length k of known pilot symbols, with μ optimized before transitioning to a decision-directed (blind) mode of operation.

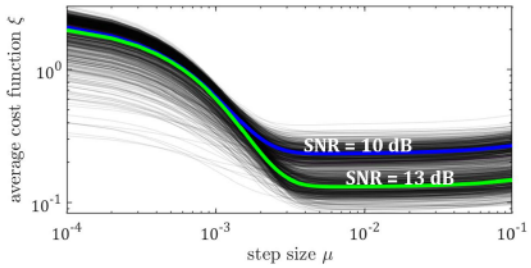


Fig. 13. Averaged final cost $\bar{\xi}$ over 500 fiber rotation trials with varying SNR, using 1,000 pilot symbols. Plotted as a function of step size μ.

5.2.2. Pilot-based polarization derotation using the pseudo-inverse

The Wiener-Hopf equation and the pseudo-inverse yield equivalent solutions, as shown by the mathematical identity of Eqs. (29) and (41). The approximation $\mathbf{R}^{-1}\vec{t}_k \approx \hat{s}_k$ is further clarified through the ensemble averaging inherent in the Wiener-Hopf formulation.

Since the pseudo-inverse relies on averaging over symbol ensembles, its accuracy degrades with shorter pilot sequences. This motivates an experimental evaluation using the 4-SVM simplex constellation.

A dual-polarization IQ transmitter driven by user-defined waveforms from an external arbitrary waveform generator (AWG) is used. The data payload is based on a 4^5 De Bruijn sequence, prefixed by k pilot symbols selected from the orthogonal Stokes basis $[1,0,0]^T$, $[0,1,0]^T$, and $[0,0,1]^T$, repeated cyclically. The full experimental setup is shown in Fig. 14. The transmitter consists of an AWG, a continuous-wave (CW) laser, a 1:2 optical splitter, two quadrature modulators (QMs), and a polarization beam combiner (PBC). Due to the lack of a Stokes vector receiver, a coherent intradyne receiver captures both quadratures of each polarization of the 4-SVM signal. The coherent intradyne architecture mixes the incoming signal with a local oscillator (LO), and the resulting waveforms are captured using a four-channel oscilloscope,

Optics EXPRESS

which then feeds the data into the DSP block. The SVM simplex optimization experiment was performed at a symbol rate of 4.6 GBd.

To facilitate the derotation, each oscilloscope record captures a full sequence of symbols including both pilot and payload packets. An additional guard band of a single repeated symbol is used as an identifier signifying the beginning of the pilot band, Fig. 15.

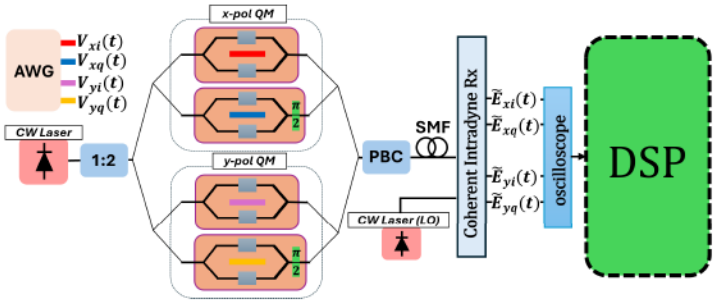


Fig. 14. Block diagram for the simplex SVM optimization experiment.

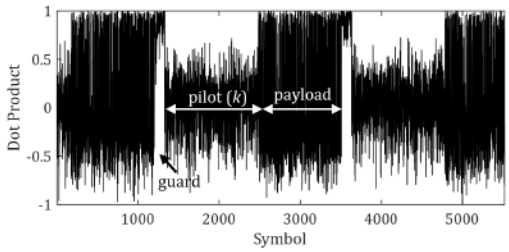


Fig. 15. Successive symbol dot products with pilot symbol length $k = 1{,}152$ and a 4-SVM payload.

Poincaré sphere visualizations in Figs. 16(a) and 16(b) show received Stokes vectors from three consecutive acquisitions with pilot lengths $k = 3$ and $k = 1{,}152$, respectively.

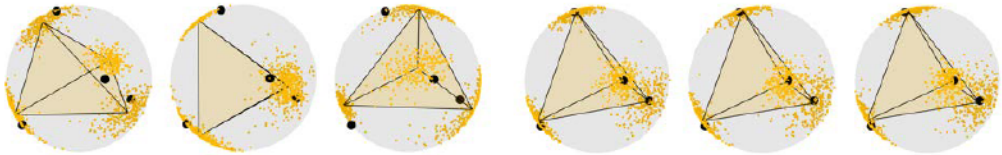


Fig. 16. Poincaré sphere visualizations of derotated Stokes vectors following three consecutive acquisitions with (a) $k = 3$ and (b) $k = 1{,}152$ after implementing the pseudo-inverse. The tetrahedra are formed using the averages of each group of received Stokes vectors (orange) and the black points represent the ideal symbol vertices.

As anticipated, improved rotational consistency is observed with the longer pilot sequence. Due to the inconsistency of rotations where $k = 3$, we find a substantial penalty incurred at the KP4 FEC threshold of approximately 3 dB to that of $k = 1{,}152$, Fig. 17. Additionally, we found for $k \geq 96$, the BER results converge to the $k = 1{,}152$ curve with negligible penalty.

Optics EXPRESS

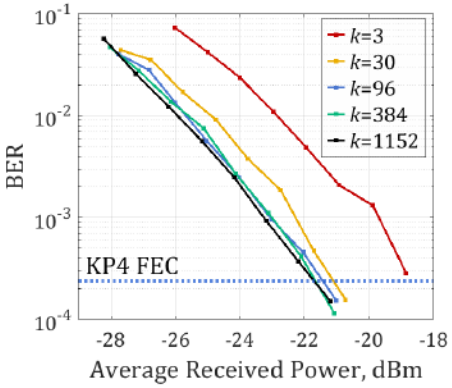


Fig. 17. BER vs average received power for different pilot lengths k at a symbol rate of 4.6 GBd.

6. Summary

The demand for Tb/s-class Ethernet optical interconnects has spurred renewed interest in advanced modulation formats and direct-detection (DD) receiver architectures. Among various DD designs, Stokes Vector Modulation with direct detection (SVM/DD) has gained prominence due to its ability to encode information on both the x and y states of polarization simultaneously and follow polarization variations using simplified MIMO-based polarization tracking. While SVM/DD systems offer improved energy efficiency compared to conventional amplitude modulation, their performance is ultimately limited by the dimensionality of the signal space.

In parallel, the adoption of multicore fibers in datacenters has opened new possibilities for increasing the capacity of short-haul optical links. Although typically used for space-division multiplexing (SDM), MCFs offer multiple spatial and polarization degrees of freedom that can alternatively be exploited jointly to transmit a single data stream more efficiently.

In recent papers, we presented Mode Vector Modulation (MVM)—a novel spatial modulation format that generalizes SVM to multimode links. MVM enables the use of a digital polarimetric DD receiver that extends the single-mode Stokes vector receiver to higher-dimensional generalized Stokes spaces. In [17], we showed that geometric shaping of MVM constellations leads to superior receiver sensitivity and energy efficiency relative to both SVM/DD and M-PAM/DD formats. Performance gains, measured in terms of SNR improvements, scale with the number of spatial degrees of freedom.

This paper proposes several new MVM transceiver architectures with linear hardware complexity and Stokes-space-based algorithms for polarization tracking. We provide theoretical and experimental back-to-back results for thermal-noise-limited and optically pre-amplified MVM/DD receivers considering the impact of various transmission impairments in a FMF. These results demonstrate MVM's potential as a replacement for conventional PAM4/DD optical transponders in short-haul optical links.

Funding. Air Force Research Laboratory (FA8750-20-1-1004, FA8750-23-2-0500).

Acknowledgment. The authors are thankful to Drs. J. Kwapisz and E. Fink of Montana State University for fruitful discussions. Finally, the authors appreciate the assistance of Montana State University PhD graduate student A. Rahman with the preparation of the manuscript.

Disclosures. The authors declare no conflicts of interest.

Data availability. The data underlying the numerical and experimental results presented in this paper are available from the corresponding author upon reasonable request.

References

Optics EXPRESS

1. Ethernet Alliance, "2025 Ethernet Roadmap: The Past, Present and Future of Ethernet," https://ethernetalliance.org/technology/ethernet-roadmap/ (2025). [Online].
2. C. St-Arnault, R. Gutiérrez-Castrejón, S. Bernal, *et al.*, "Practical fiber dispersion-induced limitations for 1.6 Tbps (4× 400 Gbps/λ) O-band IM/DD transmission systems over 2, 10, 20 and 40 km," J. Lightwave Technol. **43**(7), 3222–3232 (2025).
3. H. Zhou, Y. Li, Y. Liu, *et al.*, "Recent advances in equalization technologies for short-reach optical links based on PAM4 modulation: A review," Appl. Sci. **9**(11), 2342 (2019).
4. R. Nagarajan, I. Lyubomirsky, and O. Agazzi, "Low power DSP-based transceivers for data center optical fiber communications (invited tutorial)," J. Lightwave Technol. **39**(16), 5221–5231 (2021).
5. R. Nagarajan, A. Martino, D. A. Morero, *et al.*, "Recent advances in low-power digital signal processing technologies for data center applications," J. Lightwave Technol. **42**(12), 4222–4232 (2024).
6. D. V. Plant, M. H. Morsy-Osman, M. Chagnon, *et al.*, "Trends in high-speed interconnects for datacenter networking: Multidimensional formats and their enabling DSP," in *Optical Switching in Next Generation Data Centers*, (Springer, 2018), pp. 261–277.
7. X. Chen, C. Antonelli, A. Mecozzi, *et al.*, "High-capacity direct-detection systems," in *Optical Fiber Telecommunications VII*, (Elsevier, 2020), pp. 419–441.
8. J. K. Perin, A. Shastri, and J. M. Kahn, "Coherent data center links," J. Lightwave Technol. **39**(3), 730–741 (2021).
9. H. Liu, C. F. Lam, and C. Johnson, "Scaling optical interconnects in datacenter networks opportunities and challenges for WDM," in *IEEE Symposium on High Performance Interconnects*, (2010), pp. 113–116.
10. Q. Cheng, M. Bahadori, M. Glick, *et al.*, "Recent advances in optical technologies for data centers: a review," Optica **5**(11), 1354–1370 (2018). Publisher: Optica Publishing Group.
11. G. M. Saridis, D. Alexandropoulos, G. Zervas, *et al.*, "Survey and evaluation of space division multiplexing: From technologies to optical networks," IEEE Commun. Surv. Tutorials **17**(4), 2136–2156 (2015).
12. T. Hayashi, T. Nagashima, T. Morishima, *et al.*, "Multi-core fibers for data center applications," in *45th European Conference on Optical Communication (ECOC 2019)*, (2019), pp. 1–4.
13. T. A. Eriksson, P. Johannisson, B. J. Puttnam, *et al.*, "*K*-over-*L* multidimensional position modulation," J. Lightwave Technol. **32**(12), 2254–2262 (2014).
14. B. J. Puttnam, T. A. Eriksson, J.-M. D. Mendinueta, *et al.*, "Modulation formats for multi-core fiber transmission," Opt. Express **22**(26), 32457 (2014).
15. B. Puttnam, J.-M. D. Mendinueta, R. S. Luís, *et al.*, "Energy efficient modulation formats for multi-core fibers," in *2014 OptoElectronics and Communication Conference and Australian Conference on Optical Fibre Technology*, (IEEE, 2014), pp. 694–696.
16. B. J. Puttnam, R. S. Luis, E. Agrell, *et al.*, "High capacity transmission systems using homogeneous multi-core fibers," J. Lightwave Technol. **35**(6), 1157–1167 (2017).
17. J. Kwapisz, I. Roudas, and E. Fink, "Mode vector modulation: Extending Stokes vector modulation to higher dimensions," J. Lightwave Technol. **42**(6), 1966–1990 (2024).
18. J. Proakis, *Digital communications* (McGraw-Hill, Boston, 2008).
19. J. Kwapisz, I. Roudas, and E. Fink, "Error probability of mode vector modulation optically-preamplified direct-detection receivers," in *Conference on Lasers and Electro-Optics (CLEO)*, (2022). Paper SM4J.1.
20. I. Roudas and J. Kwapisz, "Stokes Space Representation of Modal Dispersion," IEEE Photonics J. **9**(5), 1–15 (2017).
21. J. Kwapisz, I. Roudas, E. Fink, *et al.*, "Mode vector modulation direct-detection receivers with linear hardware complexity," in *IEEE Photonics Conference (IPC)*, (2022). Paper TuF1.3.
22. S. Betti, F. Curti, G. De Marchis, *et al.*, "Multilevel coherent optical system based on Stokes parameters modulation," J. Lightwave Technol. **8**(7), 1127–1136 (1990).
23. S. Benedetto and P. Poggiolini, "Theory of polarization shift keying modulation," IEEE Trans. Commun. **40**(4), 708–721 (1992).
24. S. Benedetto and P. Poggiolini, "Multilevel polarization shift keying: optimum receiver structure and performance evaluation," IEEE Trans. Commun. **42**(2/3/4), 1174–1186 (1994).
25. S. Benedetto, R. Gaudino, and P. Poggiolini, "Direct detection of optical digital transmission based on polarization shift keying modulation," IEEE J. Select. Areas Commun. **13**(3), 531–542 (1995).
26. K. Kikuchi and S. Kawakami, "Multi-level signaling in the Stokes space and its application to large-capacity optical communications," Opt. Express **22**(7), 7374 (2014).
27. S. S. Cercós, M. Piels, J. Estarán, *et al.*, "100 Gbps IM/DD links using quad-polarization: Performance, complexity, and power dissipation," Opt. Express **23**(15), 19954 (2015).
28. D. Che, A. Li, X. Chen, *et al.*, "Stokes vector direct detection for linear complex optical channels," J. Lightwave Technol. **33**(3), 678–684 (2015).
29. D. Che and W. Shieh, "Polarization demultiplexing for Stokes vector direct detection," J. Lightwave Technol. **34**(2), 754–760 (2016).
30. P. Dong, X. Chen, K. Kim, *et al.*, "128-Gb/s 100-km transmission with direct detection using silicon photonic Stokes vector receiver and I/Q modulator," Opt. Express **24**(13), 14208 (2016).
31. M. Morsy-Osman, M. Chagnon, and D. V. Plant, "Four-dimensional modulation and Stokes direct detection of polarization division multiplexed intensities, inter polarization phase and inter polarization differential phase," J. Lightwave Technol. **34**(7), 1585–1592 (2016).

Optics EXPRESS

32. M. Chagnon, M. Morsy-Osman, D. Patel, *et al.*, "Digital signal processing for dual-polarization intensity and interpolarization phase modulation formats using Stokes detection," J. Lightwave Technol. **34**(1), 188–195 (2016).
33. M. Chagnon, M. Morsy-Osman, and D. V. Plant, "Multi-dimensional formats and transceiver architectures for direct detection with analysis on inter-polarization phase modulation," J. Lightwave Technol. **35**(4), 885–892 (2017).
34. M. Y. S. Sowailem, T. M. Hoang, M. Morsy-Osman, *et al.*, "Impact of chromatic dispersion compensation in single carrier two-dimensional Stokes vector direct detection system," IEEE Photonics J. **9**(4), 1–10 (2017).
35. S. Ishimura and K. Nishimura, "DSP technologies in the Stokes vector receivers for short-reach optical transmission systems," in *Metro and Data Center Optical Networks and Short-Reach Links*, M. Glick, A. K. Srivastava, and Y. Akasaka, eds. (SPIE, 2018).
36. S. Ghosh, T. Tanemura, Y. Kawabata, *et al.*, "Decoding of multilevel Stokes-vector modulated signal by polarization-analyzing circuit on InP," J. Lightwave Technol. **36**(2), 187–194 (2018).
37. T. Hoang, M. Sowailem, Q. Zhuge, *et al.*, "Enabling high-capacity long-reach direct detection transmission with QAM-PAM Stokes vector modulation," J. Lightwave Technol. **36**(2), 460–467 (2018).
38. T. Tanemura and Y. Nakano, "Compact InP Stokes-vector modulator and receiver circuits for short-reach direct-detection optical links," IEICE Trans. Electron. **E101.C**(7), 594–601 (2018).
39. M. Morsy-Osman, M. S. Alam, K. A. Shahriar, *et al.*, "Optimum three-dimensional constellations for Stokes vector direct detect receivers," IEEE Photonics Technol. Lett. **31**(8), 587–590 (2019).
40. S. Ghosh, T. Suganuma, S. Ishimura, *et al.*, "Complete retrieval of multi-level Stokes vector signal by an InP-based photonic integrated circuit," Opt. Express **27**(25), 36449 (2019).
41. S. Ishimura, K. Nishimura, Y. Nakano, *et al.*, "Polarization-diversity Stokes-analyzer-based coherent receiver," Opt. Express **27**(6), 9071 (2019).
42. N. Cui, Z. Zheng, X. Zhang, *et al.*, "Joint blind equalization of CD and RSOP using a time-frequency domain Kalman filter structure in Stokes vector direct detection system," Opt. Express **27**(8), 11557 (2019).
43. K. Kikuchi, "Sensitivity analysis of optically preamplified Stokes-vector receivers using analytically derived formulae for bit-error rate," Opt. Express **28**(18), 26007 (2020).
44. T. Tanemura, T. Suganuma, and Y. Nakano, "Sensitivity analysis of photonic integrated direct-detection Stokes-vector receiver," J. Lightwave Technol. **38**(2), 447–456 (2020).
45. J. Huo, X. Zhou, C. Shang, *et al.*, "Theoretical and numerical analyses for PDM-IM signals using Stokes vector receivers," Sci. China Inf. Sci. **63**(10), 202307 (2020).
46. Y. Jin, D. Li, P. Yi, *et al.*, "Adaptive blind Stokes-space based equalizer for RSOP in SV-DD systems with high chromatic dispersion tolerance," IEEE Photonics J. **12**(2), 1–13 (2020).
47. M. Wen, B. Zheng, K. J. Kim, *et al.*, "A survey on spatial modulation in emerging wireless systems: Research progresses and applications," IEEE J. Select. Areas Commun. **37**(9), 1949–1972 (2019).
48. C. Antonelli, A. Mecozzi, M. Shtaif, *et al.*, "Stokes-space analysis of modal dispersion in fibers with multiple mode transmission," Opt. Express **20**(11), 11718–11733 (2012).
49. I. Roudas, J. Kwapisz, and D. A. Nolan, "Optimal launch states for the measurement of principal modes in optical fibers," J. Lightwave Technol. **36**(20), 4915–4931 (2018).
50. Y. Zhao, C. Doerr, F. Liu, *et al.*, "425-Gbps/? Dual-polarization IMDD Transceiver," (2025).
51. D. Divsalar and M. Simon, "Multiple-symbol differential detection of MPSK," IEEE Trans. Commun. **38**(3), 300–308 (1990).
52. M. Nazarathy and E. Simony, "Multichip differential phase encoded optical transmission," IEEE Photonics Technol. Lett. **17**(5), 1133–1135 (2005).
53. I. Roudas, E. Fink, and J. Kwapisz, "Geometrically-shaped multichip DPSK," in *2024 IEEE Photonics Conference (IPC)*, (2024), pp. 1–2.
54. D. Che, A. Li, X. Chen, *et al.*, "160-Gb/s Stokes vector direct detection for short reach optical communication," in *2014 Optical Fiber Communication Conference (OFC)*, (2014), pp. 1–3.
55. W. Shieh, H. Khodakarami, D. Che, *et al.*, "Polarization diversity and modulation for high-speed optical communications: architectures and capacity," APL Photonics **1**(4), 040801 (2016).
56. A. Biswas, I. Roudas, J. Kwapisz, *et al.*, ""Low-complexity Direct-Detection Polarimetric Receiver for Mode Vector Modulation," in 2025 IEEE International Conference on Communications (ICC), (2025), pp. 2217–2223.
57. A. Biswas, I. Roudas, J. Kwapisz, *et al.*, "Cost-efficient Direct-Detection Mode Vector Receiver," in 2025 Conference on Lasers and Electro-Optics (CLEO), (2025), pp. 1–2.
58. S. Huard, *Polarization of light* (Wiley, 1997).
59. B. Farhang-Boroujeny, *Adaptive Filters: Theory and Applications* (Wiley, 2013), 2nd ed.
60. F. M. Ferreira, C. S. Costa, A. D. Ellis, *et al.*, "Semi-analytical modelling of linear mode coupling in few-mode fibers," J. Lightwave Technol. **35**(18), 4011–4022 (2017).
61. M. Morsy-Osman, M. Chagnon, M. Poulin, *et al.*, "224-Gb/s 10-km transmission of PDM PAM-4 at 1.3 μm using a single intensity-modulated laser and a direct-detection MIMO DSP-based receiver," J. Lightwave Technol. **33**(7), 1417–1424 (2015).
62. F. Ferreira, D. Fonseca, and H. Silva, "Design of few-mode fibers with arbitrary and flattened differential mode delay," IEEE Photonics Technol. Lett. **25**(5), 438–441 (2013).